The Transverse Crack Tension test revisited
An experimental and numerical study

Scalici, T.; Pitarresi, G.; Catalanotti, G.; van der Meer, F. P.; Valenza, A.

DOI
10.1016/j.compstruct.2016.09.033

Publication date
2016

Document Version
Proof

Published in
Composite Structures

Citation (APA)
Scalici, T., Pitarresi, G., Catalanotti, G., van der Meer, F. P., & Valenza, A. (2016). The Transverse Crack Tension test revisited: An experimental and numerical study. *Composite Structures*, *158*, 144-159. https://doi.org/10.1016/j.compstruct.2016.09.033

Accepted Manuscript

The Transverse Crack Tension test revisited: an experimental and numerical study

T. Scalici, G. Pitarresi, G. Catalanotti, F.P. van der Meer, A. Valenza

PII: S0263-8223(16)30613-4
DOI: http://dx.doi.org/10.1016/j.compstruct.2016.09.033
Reference: COST 7759

To appear in: *Composite Structures*

Received Date: 15 May 2016
Revised Date: 12 September 2016
Accepted Date: 13 September 2016

Please cite this article as: Scalici, T., Pitarresi, G., Catalanotti, G., van der Meer, F.P., Valenza, A., The Transverse Crack Tension test revisited: an experimental and numerical study, *Composite Structures* (2016), doi: http://dx.doi.org/10.1016/j.compstruct.2016.09.033

The Transverse Crack Tension test revisited: an experimental and numerical study

T. Scalici [a], G. Pitarresi [b], G. Catalanotti [c,d,*], F.P. van der Meer [e], A. Valenza [a]

[a] *Università degli Studi di Palermo, DICAM, Viale delle Scienze, 90128 Palermo, Italy*

[b] *Università degli Studi di Palermo, DICGIM, Viale delle Scienze, 90128 Palermo, Italy*

[c] *INEGI, Rua Dr. Roberto Frias, 400, 4200-465 Porto, Portugal*

[d] *School of Mechanical and Aerospace Engineering, Queen's University Belfast, Belfast BT9 5AH, UK*

[e] *Faculty of Civil Engineering and Geosciences, Section of Structural Mechanics, Delft University of Technology, P.O. Box 5048, 2600 GA Delft, The Netherlands*

Abstract

Several problems arise when measuring the mode II interlaminar fracture toughness using a Transverse Crack Tension specimen; in particular, the fracture toughness depends on the geometry of the specimen and cannot be considered a material parameter. A preliminary experimental campaign was conducted on TCTs of different sizes but no fracture toughness was measured because the TCTs failed in an unacceptable way, invalidating the tests. A comprehensive numerical and experimental investigation is conducted to identify the main causes of this behaviour and a modification of the geometry of the specimen is proposed. It is believed that the obtained results represent a significant contribution in the understanding of the TCT test as a mode II characterization procedure and, at the same time, provide new guidelines to characterize the mode II crack propagation under tensile loads.

Key words: Delamination, Fracture Toughness, Numerical analysis, Experimental methods

* Corresponding author
Email address: g.catalanotti@qub.ac.uk (G. Catalanotti).

1 Introduction

Interlaminar fracture toughness is a key parameter used not only for the material screening and qualification of composite material systems, but also as an input parameter for delamination in progressive failure analysis. Delamination is, without any doubt, the most characteristic failure mode of composite laminates. Interlaminar cracks emanate from free edges, holes, open cutouts; sometimes they are originated by manufacturing defects or voids at the interface between two adjacent plies. When an interlaminar crack propagates, due to static or fatigue loads, the laminate loses its structural integrity; in the case of aeronautic structures this represents a serious air safety concern. Delamination issues are currently faced during the design of aircrafts and they have been taken on also in the Boeing 787 and in the Airbus A350 programs.

Even though the problem of delamination has been widely investigated, preventing the onset and propagation of interlaminar cracks in aeronautic structures still remains a challenging question. Indeed, although several advanced strength analysis methods for delamination have been proposed [1–5], there is still a lack of confidence concerning their numerical predictions.

One source of error is certainly given by the experimental properties used as input for the failure analysis models, and especially, the interlaminar fracture toughness. Numerous experimental procedures have been proposed to measure the interlaminar fracture toughness; the most popular are: i) the Double Cantilever Beam (DCB) [6] test method for mode I propagation, ii) the End Notched Flexural (ENF) [7], the Calibrated End-Loaded Split (C-ELS) [8], and the Transverse Crack Tension (TCT) test methods for mode II propagation, and iii) the Mixed Mode Bending (MMB) [9] test method for mixed mode propagation.

It should be observed that those experimental procedures have been developed during the last forty years and they have had all different histories. The first to be adopted by the American Society for Testing and Materials (ASTM) was the DCB test procedure [6], early in the 1994. This standard was revised and improved throughout the years and its last version is dated from 2013. More recently, in 2001, the MMB test procedure [10], was included in the ASTM standard [9]; its last revision dates from 2013. The ENF test procedure has been surrounded with more controversy; proposed since the mid 80's, when first round robin was performed, it was finally adopted only in 2014 after a long development [11–14]. The ELS End-Loaded Split (ELS) specimen too was standardized after the extensive work done by the ESIS TC4 committee.

[... PARAGRAPH REMOVED IN THE REVISED MANUSCRIPT ...]

[... PARAGRAPH REMOVED IN THE REVISED MANUSCRIPT ...]

On the other hand, the TCT test, despite its simplicity, has not been standardized because of the several questions still open that limite its use.

First of all, the measurement of the interlaminar fracture toughness in mode II, $\mathcal{G}_{IIc}$, is strongly sensitive to the test method employed. The TCT test tends to overestimate the interlaminar fracture toughness with respect to the ENF. This phenomenon was observed by several authors [15–17] and it is still not fully understood.

Moreover, the fracture toughness measured by the TCT depends on the geometry of the specimen. As pointed out by Wisnom [18] and Cui et al. [19], the measured fracture toughness depends on the total thickness of the specimen. Observing that the values of fracture toughness and of the crack propagation stability are affected by the geometry of the specimen, they suggested not to consider the fracture toughness a material property because it strongly depends on the geometry of the specimen. They concluded that *caution needs to be exercised in using values of fracture energy in situations different from the ones under which they were measured* [18]. The cause for the size effect has been investigated numerically by Van der Meer and Sluys [20].

However, the TCT is an attractive method for the aeronautic industry because it is as simple to perform as a tensile test while ASTM D7905 [7] requires several repetitions of three point bending loadings at different crack lengths for calibration purposes. Moreover, the TCT test provides a measurement of delamination fracture toughness in laminates loaded in tension. There are different realistic scenarios in which mode II delamination takes place in a laminate loaded in tension, such as around bolted joints, near ply terminations and near matrix cracks. The stress state in the TCT specimen closely resembles the stress state around the growing delamination crack in these scenarios. The differences in $\mathcal{G}_{IIc}$ measurements between the ENF and the TCT are therefore relevant for accurate prediction of mode II delamination in laminates loaded in tension. In this paper, the TCT specimen is investigated experimentally and numerically with the aim of understanding the nature and sequence of the different dissipative phenomena that take place during the interlaminar crack propagation. Those collateral dissipative phenomena interact with the interlaminar crack propagation, and, if not properly taken into account, may conduct to a misleading interpretation of the actual failure mechanisms involved, with the consequence of invalidating the experimental procedure itself.

To the best of our knowledge, a lack in the direct experimental observation of the fracture onset and propagation in a TCT specimen exists in literature. With the aim of assessing the validity and robustness of the TCT test, several experimental techniques are used in this work. Two different non-contact full field methods, the Digital Image Correlation (DIC) and the Thermoelastic

Stress Analysis (TSA), are used to investigate respectively the strain and stress fields in the close-to-crack area. In addition to this, a detailed description of the morphology of the sample is reported with the support of macrograph and Micro Computed Tomography (Micro-CT) images. The analysis of the fracture surfaces is done through Scanning Electron Microscopy (SEM).

It is concluded that several parameters play an important role and may invalidate the experimental procedure. To mitigate these sources of error, a slight change in the geometry of the specimen is proposed and investigated. It is demonstrated that the proposed modification heavily reduces the collateral phenomena that accompany the interlaminar crack propagation in the classical TCT specimen.

It is believed that the obtained results represent a significant contribution in the understanding of the TCT test as a mode II characterization procedure and, at the same time, provide new guidelines to characterize the mode II crack propagation under tensile loads, an issue scarcely investigated.

2 Materials and methods

2.1 Materials

Samples were manufactured using unidirectional Hexcel IM7-8552 prepregs with a nominal ply thickness (after curing) of 0.125 mm. The mechanical properties of the unidirectional lamina are reported in Table 1.

[Table 1 about here.]

Unidirectional plates with in plane dimensions of 300×300 mm^2 were manufactured with the layup, $[0_n/\tilde{0}_{2n}/0_n]$, where the tilde denotes the cut plies. $n = 3, 6, 8, 9$ was used corresponding to laminate nominal thickness of 1.5 mm, 3.0 mm, 4.0 mm, and 4.5 mm, respectively. Prepregs were cut using a rotary cutter and placed on top of another to obtain the desired layup. The material was cured in hot press according to the suppliers specification [21] and specimens were cut, using a water-cooled diamond blade saw, to their nominal dimensions of 20×200 mm^2. The nominal geometry of the TCT sample is reported in Figure 1.

2.2 Specimens morphology and Scanning Electron Microscopy

The pristine specimens were macroscopically analysed through digital image macro observation using a 24.1 MPixel single-lens digital reflex camera with a 60 mm macro lens. Micro computed tomography (CT) was performed to evaluate the morphology of the region of interest (i.e. close-to-crack area). The X ray scanning was executed through the High-resolution micro-CT, SKYSCAN 1272 by Bruker (United States) setting a rotation angle of 180° with a rotation step of 0.4°. The voltage was set to 60 kV with a 0.25 mm aluminium filter. The acquired scans were post processed to obtain a 3D image.

Scanning electron microscope observations on fracture planes were done on the failed specimens to analyze the morphology of the surfaces after propagation of the crack. In particular, the close-to-crack area was mechanically extracted from the tested samples and Scanning Electron Microscopy (SEM) was performed using SEM Phenom World model Phenom Pro X. In the case of CFRP, gold coating was not necessary to obtain a good image quality because of the electroconductivity of the carbon fibres.

2.3 Digital Image Correlation

A 2D-DIC analysis was performed using an in house system coupled with both a Matlab-based software (i.e. Ncorr [22]) and an open source tethering software for the camera triggering control. Table 2 shows the parameters and the main technical data of the hardware used.

[Table 2 about here.]

DIC analysis was carried out during quasi-static tensile tests, loading the sample in a MTS 810 servo-hydraulic testing machine. The cross-head speed was set to 2 mm/min and the load vs. displacement curve was recorded. Prior to testing the specimen were painted with a matt white paint on top of which the speckle was made using a matt black paint [23]. The proven ability of the DIC in dealing with crack propagation in fibre reinforced composites was demonstrated in [24–26].

2.4 Thermoelastic Stress Analysis

A TSA setup is implemented to acquire the thermoelastic signal over the thickness face of TCT samples [27]. This technique is here chosen for a number of potential outcomes of particular interest for the evaluation of a TCT configuration. These comprise: the experimental evaluation of a full field stress function that develops peculiar values when a pure shear mode or a stress component in the fibres transverse direction are developed, the possibility to use the same stress function to evaluate the ability of a manufactured (and hence defect prone) TCT sample in reproducing the expected stress distribution, the possibility to detect mechanical dissipation energy effects and the sites where this may arise. Samples for TSA have been tested under sinusoidal load cycling in a MTS 810 servo-hydraulic testing machine. The temperature during cycling was measured by a FLIR X6540sc IR camera. This thermographic camera is equipped with a cooled InSb focal plane array sensor of 640×512 pixels, capable of a thermal resolution (Noise Equivalent Temperature Difference) of 18 mK. The optical setup of the IR camera comprises a 50 mm $f/2$ lens and a 12 mm extension ring. This combination allowed to achieve a maximum spatial resolution (IFOV) of about 70 μm/pixel.

The temperature variation ΔT at the loading frequency is referred to as the thermoelastic signal [28,29]. For a generic orthotropic material, with principal material directions indicated by subscripts 1 and 3, it is described by the following linear stress function [30,31]:

$$\Delta T = -\frac{T_0}{\rho C_p} \left(\alpha_1 \Delta\sigma_1 + \alpha_3 \Delta\sigma_3 \right) \tag{1}$$

where ΔT is the thermoelastic effect induced temperature variation, T_0 is the absolute sample temperature, ρ and C_p are the homogenized bulk material density and specific heat, $\alpha_{1,3}$ are the principal material coefficients of thermal expansion (CTE) in longitudinal and thickness direction, and $\sigma_{1,3}$ are the corresponding stress components.

In this paper the thermoelastic signal is obtained by two equivalent off-line Lock-In procedures: i) the commercial software THESA by Flir, which uses a physical reference signal representative of the loading frequency, and ii) a custom Fourier Transform based Matlab routine written by the authors [32], which uses a reconstructed reference signal. Both analyses were performed in parallel allowing to cross-check the uniqueness and reliability of the determined thermoelastic signal. The thermogram sequences processed by the lock-in procedures were acquired over a time window of 32 s with a sampling frame rate of 64 Hz. The only sample preparation consisted in painting the sample thickness side with three passes of a RS matt black paint.

Some preliminary considerations are given about the expected output of the TSA analysis. The Lock-In analysis is able to provide both the amplitude and phase of the thermoelastic signal, being this the harmonic of the temperature/time signal at the loading frequency [24,32]. Hence the thermoelastic signal can be represented as a trigonometric function as follows:

$$S = A\left(\cos\omega t + \varphi\right) \tag{2}$$

with $A = \Delta T$ and

$$\varphi = \begin{cases} \alpha + 0^\circ & \text{if } \alpha_1\Delta\sigma_1 + \alpha_3\Delta\sigma_3 < 0 \\ \alpha + 180^\circ & \text{if } \alpha_1\Delta\sigma_1 + \alpha_3\Delta\sigma_3 > 0 \end{cases} \tag{3}$$

where α is a generic shift angle between the sinusoidal loading and the triggering time of the temperature sampling. In the case of adiabatic conditions, φ can assume two different values that differ by 180° corresponding to a different sign of the stress function $\alpha_1\Delta\sigma_1 + \alpha_3\Delta\sigma_3$.

In the case of a CFRP TCT sample, two main stress field scenarios are expected. The zones far from the transverse crack should experience a prevalent uniaxial stress field with $\sigma_1 \neq 0$ and $\sigma_3 = \tau_{13} = 0$. The zones near the transverse crack tips are expected to develop a pure shear stress mode, with $\sigma_1 = \sigma_3 = 0$ and $\tau_{13} = \tau_{max}$ (notice that in this notation 1,2,3 represent the principal material and not the principal stress directions). In the second case the thermoelastic signal should be null, while in the first case a very low thermoelastic signal is expected, due to the typically low values of α_1 for CFRPs [30]. Table 1 reports values of the CTEs for the analysed material, confirming that α_3 is almost an order of magnitude bigger than α_1. It is also observed that α_1 is negative for the specific CFRP studied, so zones under prevalent uniaxial stress should develop a temperature variation ΔT in phase with the load, i.e. ΔT increases when the load increases. One potential perspective of the present technique is that any departures from a pure shear or uniaxial stress state should be highlighted by a significant enhancement of the thermoelastic signal. In fact, such departures both imply that a σ_3 component arises. Since σ_3 is naturally amplified by the coefficient $\alpha_3 >> |\alpha_1|$, its presence should enhance the thermoelastic signal. Furthermore if a positive σ_3 component arises such that $\alpha_3\Delta\sigma_3 \geq |\alpha_1\Delta\sigma_1|$, a 180° change in phase should also be observed in the thermoelastic signal.

In this work the lock-in filtering is also performed at twice the loading frequency. The such obtained amplitude map is here called Second Harmonic signal. This information can be correlated with the presence of energy dissipation as proposed in [33] and exploited by some authors [34,35].

2.5 Numerical analysis

The Energy Release Rate (ERR) of a TCT specimen (see Figure 1) is computed using a simple analytical model based on energetic balance as:

$$\mathcal{G}_{II} = \sigma^2 \frac{H}{2E_1} \left(\frac{1}{\eta} - 1 \right) \tag{4}$$

where σ is the remote stress, $2H$ is the thickness of the specimen, E_1 the Young's modulus in the longitudinal direction of the specimen, and η is the cut factor, $\eta = \hat{H}/H$, defined as the ratio between the thickness of the uncut plies, $2\hat{H}$, and the thickness of the specimen, $2H$ [17].

[Fig. 1 about here.]

Equation (4) is derived with the assumption that the delamination crack length is sufficiently large for a cracked region with uniform stress distribution to exist. In that case, the energy release rate can be computed from the difference in elastic energy in cracked and uncracked regions. The solution is independent of the crack length and of the orthotropy of the material. Alternatively, the Energy Release Rate (ERR) of a crack propagating in an orthotropic body, in plane strain, can be obtained using the orthotropy rescaling technique [36,37]. This approach, based on the stress intensity factors at the crack tip, is also valid for short cracks. Let x_1,x_2 and x_3 be the coordinate system associated with the specimen. If x_1 and x_2 are also the natural axes of the material, assuming that the crack propagates in the x_1 direction, the ERR reads:

$$\mathcal{G}_{II} = \left(b_{11} b_{33} \frac{1+\rho}{2} \right)^{1/2} \lambda^{1/4} \mathcal{K}_{II}^2 \tag{5}$$

where the coefficients b_{ij} are written as function of the compliances, s_{ij}, as:

$$b_{ij} = s_{ij} - s_{i2} s_{j2} / s_{22} \tag{6}$$

and the two dimensionless parameters, λ and ρ, are defined as:

$$\lambda = b_{11}/b_{33}, \qquad \rho = \frac{2b_{13} + b_{55}}{2\sqrt{b_{11} b_{33}}} \tag{7}$$

The Stress Intensity Factor (SIF) of Equation (5) reads:

$$\mathcal{K}_{II} = \sigma \sqrt{H} \kappa \tag{8}$$

being $\kappa = \kappa\,(\alpha, \eta, \rho, \lambda, L)$ a dimensionless correction factor that takes into account the geometry of the specimen and the orthotropy of the material. α

is the normalized crack length and it is defined as $\alpha = a/H$ where a is the crack length, and $2L$ is the length of the specimen.

Substituting the SIF of Equation (8) in Equation (5) the energy release rate reads:

$$\mathcal{G}_{II} = \left(b_{11} b_{33} \frac{1+\rho}{2} \right)^{1/2} \lambda^{1/4} \sigma^2 H \kappa^2 \tag{9}$$

The correction factor can be found using the Finite Element Method (FEM). Finite Element Analyses (FEAs) were carried out in Abaqus commercial software. The two-dimensional model uses the 4-node quadratic, reduced integration element, CPE4R. The Virtual Crack Closure Technique (VCCT) [38] (implemented in a Python script) and the domain integration method [39] Abaqus built-in procedure were both used to estimate the Energy Release Rate. The VCCT allows to obtain $\mathcal{G}_I$ and $\mathcal{G}_{II}$, while the domain integral method only the total ERR, $\mathcal{G}$. The redundant information obtained from the domain integration method was used to double check the implemented algorithm.

In this paper, the ratio between thickness of the uncut plies and the total thickness of the laminate is kept constant. Moreover, under the reasonable assumption that the length of the specimen is much larger than both the thickness of the specimen and the crack length at the unstable crack propagation ($L >> a, H$), the length of the specimen, L does not play a role in the determination of the ERR. Therefore, η and L can be both eliminated from the numerical calibration and the only geometric parameter that plays a role is the crack length (a or α).

Figures 2a and 2b report respectively the mode mixity, ψ, and the correction factor κ, both as a function of the normalized crack length $\alpha = a/H$ being a the crack length. The mode mixity is defined as $\psi = \mathcal{G}_{II}/\mathcal{G}$ being $\mathcal{G}$ the total energy release rate ($\mathcal{G} = \mathcal{G}_I + \mathcal{G}_{II}$). Of course, $\psi = 0$ and $\psi = 1$ for mode I and mode II, respectively.

[Fig. 2 about here.]

Figure 2a reveals that the cracks do not propagate at pure mode II at the beginning of the crack propagation and that the condition of $\psi = 1$ (pure mode II) is reached only when $\alpha > 0.25$ (i.e. $a > 0.25H$). That means that care is required when testing thick specimens. Indeed the crack propagation in a TCT is unstable and, therefore, the peak load is reached when the crack propagation is smaller than the length of fracture process zone, l_{fpz}. Therefore, in a big specimen the unstable crack propagation could occur at mixed mode and not at pure mode II as required.

Figure 2b shows the correction factor κ as a function of α for different values of ρ and λ. The correction factor stabilizes only when the normalized crack length is larger than a threshold value, $\alpha > \alpha_t$, being $\alpha_t \approx 3$. This means that a correct determination of the fracture toughness in a TCT would require also the knowledge of the crack length when the unstable crack propagation is reached.

The steady-state value of the correction factor, $\hat{\kappa}$ can be found for $\alpha \to \infty$; as a consequence, its dependence on α can be eliminated ($\hat{\kappa} = \hat{\kappa}(\rho, \lambda)$). Figure 3 shows the values of $\hat{\kappa}$ found numerically and their fitting.

[Fig. 3 about here.]

The polynomial fitting surface employed reads:

$$\hat{\kappa} = \sum P_{ij}\, \rho^{i+1} \lambda^{j+1} \tag{10}$$

where P_{ij} is the element of the matrix $\boldsymbol{P}$ of indexes i and j. The matrix $\boldsymbol{P}$ is defined as:

$$\boldsymbol{P} = \begin{bmatrix} 0.4331 & 4.6730 & -45.68 & 1.835 \\ -0.09148 & -0.3427 & 1.102 & 0 \\ 0.02157 & 0.02272 & 0 & 0 \\ -0.001955 & 0 & 0 & 0 \end{bmatrix} \tag{11}$$

It is worth noticing that the TCT is not characterized by a *positive geometry* [40] and therefore the use of the size effect method, as already done for fibre reinforced composites [41–43], is prevented.

3 Experiments on the TCT specimen

3.1 Preliminary tests

Three lay-ups, with n=3,6, and 9 (see Section 2.1), were tested in the preliminary test campaign. Five samples per lay-up were tested at a cross-head speed of 2 mm/min and photograms of the samples were acquired. Experimental results are reported in Table 3.

[Table 3 about here.]

For the thinnest samples (i.e. 1.5 mm) net tension failure was observed before the onset of the crack propagation. For the other specimen asymmetrical cracks developed invalidating the test see Figure 4. In only one specimen a symmetrical propagation of the crack was observed. However, it is not possible to say if the cracks propagated symmetrically throughout the duration the test or if this condition of symmetry was only reached at the unstable crack propagation.

[Fig. 4 about here.]

As the specimens failed with an unacceptable failure mode, the peak loads reported, for the sake of completeness, in Table 3 cannot be used for the estimation of the interlaminar fracture toughness. It is worth noticing that the TCT test exhibit a size effect as different failure modes are observed with the change of the size of the specimen.

3.2 Specimens morphology and Micro-CT

The results obtained in the previous section shows also that a certain asymmetry arise within the specimen and this could be related with the presence of manufacturing defects in the region close to the cut.

To highlight the actual geometry of the specimens, the direct observation of the area around the cut was performed. Even if the manufacturing technique allows to obtain good quality composites, asymmetries and defects are not avoidable and represent an intrinsic characteristic of composite material systems. As shown in Figure 5a, the TCT-specimens geometry does not perfectly reproduce the theoretical model and a lack in symmetry is observed. In particular, during the curing time, the plies tend to slide one on the other under the action of the hot press causing the misalignment between the different layers leading to the formation of voids and resin pocket enclaves. In Figure 5b the defects at the crack tip are shown.

[Fig. 5 about here.]

Moreover, the pressure gradient in the thickness direction may induce a variation in the cured ply thickness resulting in differences between the two outer parts of the samples. Such irregularities may have more influence for thinner samples. Figure 6 show the experimental results of the Micro-CT analysis. The presence of resin pocket enclaves is revealed in Figure 6a (lighter zones indicated by the arrows) where the whole volume around the area is reported.

[Fig. 6 about here.]

Figure 6b reveals the presence of spherical and elongated voids. It is worth noticing that the distribution, shape and dimension of the defects is random and this may leads to scatter in the results of the mechanical analysis. Furthermore, voids and defects may affect the crack onset and propagation.

3.3 Static tests and DIC analysis

In total, 7 samples (4 mm thickness) were tested up to failure. The DIC was used to monitor the strain field and obtain important information on the crack onset and propagation.

Figure 7 reports a typical load vs. displacement curve and the apparent stiffness. It is possible to notice that the curves present a quite linear trend with a slight variation in slope (at about 14.9 kN). This variation may be attributed to the first crack propagation. However, the right load value is very difficult to be unequivocally determined because, at the unstable crack propagation, a drop in the load is not noticed; this is contrast with what reported in [17]. On the other hand, DIC analysis revealed that, the first propagation is usually not symmetrical so that it is not possible to evaluate the mode II fracture toughness using Equations (4) or (9).

[Fig. 7 about here.]

Figure 8 shows the speckled reference image (see Figure 8a) and the contour plot of the strain field ε_3 (the specimen coordinate system is reported in Section 2.5) at different loads. Asymmetries in the strain field are observed prior to the unstable crack propagation (see Figure 8b) suggesting that a stable crack propagation has already occurred. This stable crack propagation occurs at low values of load if compared to the final load drop (see Figure 8c).

[Fig. 8 about here.]

Moreover, Figure 8c shows that the crack emanates toward a single direction from a single crack tip, invalidating the test procedure. At higher load level (i.e. $\approx$ 30 kN), further non-simultaneous crack onset and propagation were observed.

Because of the asymmetry noticed in the cracks propagation, Equations (4) or (9) cannot be used to estimate the fracture toughness and their use would induce to an overestimation of the actual value of the interlaminar fracture toughness.

3.4 Scanning electron microscopy and fractography

The observation and the analysis of the close-to-crack fracture surfaces was performed on failed specimens through scanning electron microscopy. Figure 9 reports an overview of the fracture surfaces using a relatively low magnification.

Figure 9 shows an heterogeneous distribution of hackles (see Figure 9a) and regions where a thin layer of resin tends to persist after the crack onset and propagation (Figure 9b). The first ones are, usually, associated with mode II while the second one with cohesive fracture during mode I crack propagation. In particular, the predominant presence of hackles suggests a dominant mode II propagation [44,45].

Figure 9c and Figure 9d show two different areas where peeling phenomena of the layers close to the crack plane seem to occur. In Figure 9c, the highlighted pulled fibre suggests a localized fibres bridging event. Moreover, a large number of smooth surfaces corresponding to the imprints of debonded fibres is observed. Figure 9d shows out-of-plane deformations and a partially debonded fibre associated to a large area affected by cohesive failure.

Figure 9e and Figure 9f show higher magnification SEM images. In particular, in Figure 9e a portion of debonded fibre is highlighted suggesting that fibre bridging phenomena may occur. In Figure 9f, the presence of debonded fibres associated to smooth surfaces (i.e. fibre imprints) and hackles suggests a mixed mode crack propagation.

[Fig. 9 about here.]

In conclusion, SEM fractographies indicate that crack growth does not take place under pure mode II.

3.5 Thermoelastic Stress Analysis

Two nominally identical samples have been analysed with TSA, and will hereinafter be identified as `tct1` and `tct2`. Three different loading cycles have been applied: 1-9 KN, 1-11 KN and 1-17 KN, each at three different frequencies: 2, 4, 6 Hz. Figure 10 shows the amplitude of the thermoelastic signal in temperature units for two samples. The area reported in these maps is cropped upon the sample thickness, and is then 4 mm wide per 15.6 mm long, centred on the transverse cut area.

[Fig. 10 about here.]

It is first of all reported that the transverse cut in the undamaged samples is filled by cured resin, which then guarantees material continuity, although a different stiffness should characterize the central cut area from the lateral ligaments where the plies are continuous. The maps in Figure 10 refer to a condition where the central resin pocket is not broken, with the only exception of sample `tct2` tested at 1-17 kN, where such resin pocket was broken due to the high loads.

One common feature of both `tct1` and `tct2` is the very low and uniform thermoelastic signal present in most of the analysed area, both near and far from the transverse cut. This can be seen as a confirmation that a general low signal is expected due to the prevalent σ_1 dominated unidirectional stress field. Near the transverse cut tips both `tct1` and `tct2` present some local spots of high thermoelastic signal. As discussed in Section 2.4, such a high surge of thermoelastic signal can be justified by the rise of a σ_3 stress component in the transverse direction, or by a steep rise of σ_1. This last might be due to stress concentration effects induced by the transverse cut discontinuity, or to a change of the thermoelastic constant in correspondence to local resin rich pockets. Whatever the case, all above events indicate a departure from the pure shear stress field which should eventually activate a pure mode II delamination failure. Another feature of such high thermoelastic signal spots is their non-uniform distribution.

[Fig. 11 about here.]

A rather drastic increase of thermoelastic signal on the area above and below the transverse cut is observed in `tct2` when the loading amplitude is set to 1-17 KN. Figure 11 shows how such change is already observed at 2 Hz cycling, and increases in severity by moving to 4 and 6 Hz. The main reason of such change, verified by direct observation, is the onset of the transverse crack in the resin-rich pocket separating the cut plies. The formation of such crack under 1-17 kN loading occurred only in sample `tct2`, probably activated by some local weaknesses and some slight dimensional variations that differentiate sample `tct2` from `tct1`. The formation of such transverse crack was not accompanied by interlaminar fracture at the cut tips. This last failure is in fact activated by higher loads as verified by quasi-static monotonic tests (see Section 3.3). Once material continuity is lost due to the onset of the transverse cut, a surge of transverse σ_3 compressive stresses is expected to occur above and below the crack (this is typically the case in samples with centered cracks under mode I loading). The presence of such stress components is likely the reason for the steep increase of thermoelastic signal above and below the central crack. During the time window of signal sampling the high amplitude load cycle will likely introduce some further fatigue damage, but this was never seen to involve the formation of interlaminar delamination. This local progressive damage, together with dissipative heating effects, is believed to be the main reason for the different thermoelastic signal acquired in the transverse cut area with increasing loading frequency (see Figure11).

Figures 12 and 13 report the amplitude maps of the Second Harmonic Signal for sample `tct2`. Figure 12 in particular compares the second harmonic signal between the three load amplitudes: 1-9 kN, 1-11 kN and 1-17 kN at 6 Hz. It is interesting to observe that for the two lower amplitude cycles the second harmonic signal is practically null. In the case of the bigger load amplitude, i.e. the one which determined the transverse crack, it is now observed a second harmonic signal confined in the zone around the crack.

The second harmonic signal was detected also when cycling at 2 Hz and 4 Hz as shown in Figure 13. Most interestingly the second harmonic signal seems to increase with the frequency. If the second harmonic component is to be correlated to dissipative phenomena, it was observed that a big component of such dissipative effects is related to friction between single plies, with each lamina termination of the cut plies sliding upon other opposite plies during the cyclic loading. In fact, it has already been shown that the transverse cut is not straight and single plies are kind of zig-zagging and occasionally touching each other (Figure 5).

[Fig. 12 about here.]

[Fig. 13 about here.]

3.6 Concluding remarks on the TCT specimen

The TCT test procedure suffers from some important limitations.

First of all, the actual morphology and geometry of a TCT do not reproduce the theoretical model without a certain degree of uncertainty and asymmetries that, depending on their magnitude, may lead to an invalidation of the procedure itself. As observed through the DIC analysis, defects and lack of symmetry, may cause a premature crack nucleation and propagation. In such case, the analytical model can not be applied for the calculation of the critical mode II ERR.

In that regard, both the TSA and DIC analysis showed a complex triaxial stress field in the close to crack area and the not negligible presence of local transverse stresses that are not taken into account in the analytical model. The shape of the resin pocket also plays a role and this should be taken into account. Those conclusions are supported by the SEM analysis that showed the presence of some characteristic features not associated with the pure mode II crack propagation.

It should be emphasized that even if the specimen were perfect and without defects, the test could have been invalid. As showed in the numerical analysis conducted in Section 2.5, the mixed mode ratio, ψ, tends to 1 (i.e. pure mode II) only when the crack has grown substantially. Therefore the unstable crack propagation may occur at mixed mode.

Taking into account all these findings, an alternative geometry is proposed in the following.

4 A modified geometry

A new geometry, showed in Figure 14, is proposed. The idea is simple but very effective. Two release films are inserted between the cut and uncut plies creating two initials precracks. These precracks distance the crack tip from the resin pocket and remove the influence that this has on the crack tip. Moreover, having two precracks ensures (if those precracks are sufficiently long) a pure mode II crack propagation enabling the use of Equation 9 for the calculation of the ERR. Here the precracks are manufactured using a teflon film with a thickness of 0.05 mm. The thickness of the release film, t_{rf}, should not play a role for this configuration. In fact, as explained in the following, it is likely that the unstable crack propagation occur at a critical value, Δa_{crit}, that is comparable with the length of fracture process zone, l_{fpz} ($\Delta a_{crit} \approx l_{fpz}$). Since the length of the fracture process zone is much larger than the thickness of the release film, $l_{fpz} >> t_{rf}$, the crack at unstable crack propagation may be considered sharp and Linear Elastic Fracture Mechanics (LEFM) applies [46]. Furthermore, as will be shown in Section 4.2, the driving force curve for the mTCT sample, whose shape is given by Equation (9) and Figure 2(b), can reach and become tangent to the material R-curve only after the full development of the length of fracture process zone, i.e. when the R-curve is fully horizontal. From this observation it is possible to predict that the critical ERR measured from a mTCT is the steady state value of the R-curve.

[Fig. 14 about here.]

4.1 Specimens morphology and Micro-CT

Figure 15 reports the macrography of the modified geometry. Even if the transverse cut shape still remain irregular, the actual crack tips lie on a much more regular area (Figure 15a).

[Fig. 15 about here.]

Since delamination crack tips are far away from the transverse cut (Figure 15b), it is believed that the defects near the transverse cut do not influence the crack propagation.

Moreover, the CT scan reveals lower amount of defects. In particular, Figure 16 reports the area close to the crack tips. In this case, elongated defects are observed in correspondence of the release film surfaces due to the presence of the discontinuity. Moreover, no bubble shaped voids were detected and this zone results to be not disturbed by irregularities. If compared with Figure 6b, it is possible to state that the composite quality in the area around the crack tip was significantly improved, as well as the symmetry of the sample.

[Fig. 16 about here.]

4.2 Static tests and DIC analysis

Experimental tensile tests were performed on 4 samples at a load rate equal to 10 kN/min. Figure 17 reports a typical load vs. displacement curve. In the case of the new proposed configuration, no premature failure and crack onsets were detected so that the peak load can be considered as the critical load (i.e. 33.88 kN).

[Fig. 17 about here.]

DIC analysis results are reported in Figure 18. In particular, Figure 18a show the speckled reference image for the cracked zone (i.e. transverse crack and release film area). Figure 18a,b,c report the ε_3 maps at different load level. For all the cases, the release films and the transverse crack are well highlighted since they correspond to the most compliant zones. Moreover, even if the traverse crack area results to be characterized by a complex and irregular geometry, the area of interest (i.e. close to the crack tips) is homogeneous and the values of the transverse deformations ε_3 can be considered negligible until the ultimate failure. In addition to this, no premature failures were observed and four simultaneous and symmetric unstable cracks were detected.

[Fig. 18 about here.]

Considering these results, Equations (4) and (9) can be used to evaluate the interlaminar fracture toughness. Table 4 reports the mean of critical values of the energy release rate for the considered material (1.59 N/mm). It is worth noticing that using Equation (4) or (9) is indifferent and this because the crack propagates at pure mode II (outside the transition region where mixed mode occurs).

[Table 4 about here.]

It is worth comparing the value of the fracture toughness obtained in this experimental campaign, with the values reported elsewhere using the ASTM ENF procedure. In particular, experiments on the same material system were performed in [47,48]. The values reported were of 0.74 N/mm and 0.79 N/mm, in [47] and [48], respectively, when using a teflon film to create the precrack. In [47] the test was also performed on specimens where the precrack was propagated by fatigue (before testing), and the corresponding value of the fracture toughness was reported to be 1.13 N/mm. If compared with the value of the fracture toughness obtained in this work, the values obtained using the ENF are smaller especially when the precrack is created only using a release film. It is common knowledge that the unstable crack propagation occurs at the tangent point of the crack driving force curve and the R-curve, $\mathcal{G}_{IIc}\left(\Delta a\right)$; indeed, the following two conditions must be satisfied: $\mathcal{G}_{II}\left(\Delta a\right) = \mathcal{G}_{IIc}\left(\Delta a\right)$ and $\frac{\mathcal{G}_{II}(\Delta a)}{\partial \Delta a} = \frac{\mathcal{G}_{IIc}(\Delta a)}{\partial \Delta a}$. These conditions, for the TCT specimens imply that the fracture toughness estimated is the steady-state value of the R-curve, $\mathcal{G}_{IIc}^{ss}$. Indeed, the crack driving force curve of the TCT of Equation (9) is a horizontal line for $\alpha > \alpha_t$ (see Figure 2), and the only tangent point is at $\Delta a = l_{fpz}$ and $\mathcal{G}_{II} = \mathcal{G}_{IIc}^{ss}$, where l_{fpz} is the length of the fracture process zone. For the ENF, the ERR is proportional to P^2a^2 and the tangent point is expected to be at $\Delta a < l_{fpz}$ and $\mathcal{G}_{II} < \mathcal{G}_{IIc}^{ss}$, leading to a smaller value of the interlaminar fracture toughness.

4.3 Scanning electron microscopy and fractography

The direct observation of the fracture surface close to the crack tips, was done through the scanning electron microscope. Figure 19 shows two images at relatively low magnification. In Figure 19a it is possible to notice two different areas, one corresponding to the zone of the release film and the other corresponding to the fractured surface. Figure 19b shows a surface completely created by failure processes. From this last, it was assessed the presence of a homogeneous and dense distribution of hackles. The presented images confirm that the new proposed setup leads to pure mode II fracture.

[Fig. 19 about here.]

4.4 Thermoelastic stress analysis

The thermographic signal on modified TCT specimens (hereinafter referred to as `mTCT`), was acquired during both monotonic and cyclic loading. In particular, three thermograms from the monotonic loading are shown in Figure 20a.

The first thermogram was acquired at a time t^* immediately before the onset of interlaminar delamination, the second thermogram shown is immediately successive to t^*, i.e. after 0.1 s (being the sampling frequency adopted of 10 Hz), and the third after 1 sec from t^*.

[Fig. 20 about here.]

In Figure 20 the two vertical arrows indicate the terminations of the two delamination films, while the horizontal arrows point the loading direction. The thermogram at t^*+0.1s is the first acquired after the onset of delamination which occurs at the circled point of the stress/displacement curve as reported in Figure 20b. It is noteworthy to observe that the temperature of the newly delaminated area has a sudden increase on the side of the outward laminae. In fact, the extension of delamination has unloaded the central plies, suddenly transferring the whole load through the external material. The thermoelastic temperature change associated to such $\Delta\sigma_1$ jump in the external material is positive. Actually, this can be considered as an indirect proof that the α_1 of the analysed material is negative. The thermoelastic effect induced temperature change is then gradually faded due to the monotonic loading not providing adiabatic conditions. Thus the image after 1 sec already shows a homogeneous temperature distribution between inner and outer laminae. The temperature monitored during the monotonic loading has then highlighted very clearly the instant of delamination, demonstrating that the delamination itself is able to onset at a specific critical load, well identified in the load/displacement curve. Temperature mapping has also allowed to show the perfect symmetric onset of delamination failure, with four fronts of interlaminar delamination starting instantly from the four tips of the two delamination films. Additionally, as shown in Video 1, it can be seen that the failure is sudden, symmetric and with no indications of particular differences at the four crack tip sites.

The Thermoelastic and Second Harmonic Signals have been determined on an `mTCT` sample cycling between 4-21 KN, repeating the analysis at frequencies of 2,4,6 Hz. No influence of frequency was observed on the thermoelastic signal, which is shown in Fig. 16 for the 4 Hz run. By synchronizing the deformation cycle with the temperature cycle and focusing on zones of the sample under pure tensile loading (e.g. the far field or the outer laminae in the artificially delaminated zone), it was possible once again to verify that ΔT increases with $\Delta\sigma_1$, i.e. that α_1 is indeed negative.

[Fig. 21 about here.]

The amplitude map in Figure 21 shows that the outer laminae within the artificial delamination carry the whole σ_1 stress, and hence the thermoelastic signal here is higher than in the far ends of the sample, where the unidirectional stress is distributed over the whole thickness. The inner laminae (ending with the transverse cut) have a near zero thermoelastic signal. The phase signal around the transverse cut is very noisy, also due to the very low stresses. The Second Harmonic signal is almost null all over the surface, but rather interestingly, it increases along the artificial delamination, especially near the ends, probably due to some residual friction. Such trace of high Second Harmonic signal is particularly useful in revealing where the delamination films end within the sample. Some rather peculiar features of the Thermoelastic signal are observed in the zones near the artificial delamination ends. Figure 21 shows that the behavior is rather symmetrical, with a very similar signal distribution in the upper and lower delamination tips, a closer look at these zones is provided in Figure 22, focusing on one side only of the embedded delamination ends.

[Fig. 22 about here.]

Two zones of high thermoelastic signal are observed, both localized on the centre thickness area. One is found within the artificial delamination (between 5 and 7 mm from the top in Figure 22) , and one in the zone ahead of the delamination (between 9 and 13 mm from the top in Figure 22). Both are characterized by arising very near the delamination ends (which falls at about 8 mm from the top), and rapidly fading when moving away from the delamination ends. The only plausible explanation for such increase of the thermoelastic signal is the rise of a transverse σ_3 component. The zone ahead of the delamination ends is also characterized by having a 180° shift in phase compared to the pure σ_1 field zones. Therefore, it is possible to state that the zone within the delamination develops a negative σ_3, and the zone ahead of the delamination ends develops a positive σ_3. A qualitative explanation could be attempted by observing that the lateral Poisson contraction of the outer material is higher than the inner material, due to the σ_1 component concentrating towards the outer path, and this might develop some transverse stresses in the inner central zones of material where σ_1 is very low. [...] A rather peculiar and interesting feature is that the thermoelastic signal decreases to very low values right where the delamination tips are supposed to fall. This could well be due to a prevalent pure mode II stress field near the fracture process zone. Furthermore, the second harmonic signal, which could be related to friction energy dissipation, is remarkably low in amplitude, and mainly concentrated on the delamination line. It is useful to recall that the thermoelastic signal is acquired under cyclic loading between 4 and 21 kN. This is a quite intense peak-to-peak load, causing the external ligaments to stretch back and forward, while the inner sub-laminate is not deforming. It is then normal that some friction is developed between the stressed and unstressed flanks, but even so, it is very low. Considering that the fracture test is performed under slow monotonic loading, the above postulated frictional effects should be even more negligible. Furthermore, the presence of a σ_{33} compressive component closing the flanks would have induced a much higher friction and a more widespread and higher second harmonic signal. Therefore, in light of the above considerations, the thermoelastic maps provide some important hints that σ_{33} plays a marginal role in the mTCT, both in terms of crack flanks mutual compression, and in terms of a possible mixing mode arising in the fracture process zone.

5 Numerical modelling and validation

With the aim of assessing the trustworthiness of the parameter obtained using the modified TCT specimen, a numerical model was used to reproduce the experimental results. A Finite Element (FE) model of the modified TCT specimen was implemented in Abaqus [39]. Only one eighth of the specimen was modelled, taking advantage of the symmetry to reduce the computational effort. The outer and inner laminae were modelled using C3D8R brick elements with a dimension of 0.5×0.5×0.5 mm^3 while the interface was modelled using Abaqus built-in cohesive elements. Both zero-thickness and finite-thickness cohesive elements were used leading to virtually the same numerical results. In the finite-thickness elements a thickness of 0.01 mm was used following the guidelines of the Abaqus Documentation [39]. A detailed definition of the cohesive damage model may be found in [39,3] and it is not reported here for the sake of conciseness. In the following, only a description of the constitutive parameters (see Table 5) necessary for the progressive delamination model is reported.

[Table 5 about here.]

The strength in pure mode I is calculated as [4]:

$$\bar{\tau}_N = \sqrt{\frac{9\pi E \mathcal{G}_{Ic}}{32 N_e l_e}} \tag{12}$$

where E is the Young's modulus, l_e the size of the element along the direction of the crack propagation (0.5 mm), and N_e is the number of elements within the cohesive zone. Following [4] the number of the elements in the cohesive zone should be higher or equal to 3. $N_e = 5$ was used. Using Equation (12), the effective strength in pure mode I, τ_N, is calculated as [4]:

$$\tau_N = \min\left(\bar{\tau}_N, Y_T^{ud}\right) \tag{13}$$

where Y_T^{ud} is the transverse tensile strength for the unidirectional laminate ($Y_T^{ud} = 62.3$ MPa as reported in [49]). The effective shear strength, not being a fully independent material property, is calculated as [5]:

$$\tau_{sh} = \tau_N \sqrt{\mathcal{G}_{IIc}/\mathcal{G}_{Ic}} \tag{14}$$

Four different values of the fracture toughness were used here to asses the statistical quality of the analysis, and in particular:

- $\mathcal{G}_{IIc}^{ENF} = 0.79$ N/mm, corresponding to the fracture toughness obtained using the ENF test procedure by other researchers [47,48];
- $\mathcal{G}_{IIc} = 1.59$ N/mm, the value obtained in this work (see Table 4);
- $\mathcal{G}_{IIc}^{-} = 1.41$ N/mm and $\mathcal{G}_{IIc}^{+} = 1.76$, corresponding to the boundaries of the Interval of Confidence (IC) at 95% for the values of the fracture toughness reported in Table 4.

Numerical results are reported in Figure 23. In particular, Figure 23(a) reports the contour plot of the σ_{11} stress (1 is both the fibre direction and the longitudinal direction of the specimen) at the unstable crack propagation (at the first peak load) while Figure 23(b) reports the curve remote stress vs. displacement obtained. As observed the results reproduce the same behaviour obtained experimentally (see Figure 22). It should be noticed that the crack propagation is unstable at the first peak. The load does not go to zero, but increases after complete crack propagation, which is because of the constraining effect of the grips that keep together outer and inner laminae. This was modelled in Abaqus using TIE constraints, between the outer and the inner laminae, at the side of the specimen where the load is applied.

In Figure 23(b) is also reported, in light red, the 95% IC range of the peak stress. Since the error in predicting the peak load is lower than 3% we can conclude that numerical results are in excellent agreement with experiments.

[Fig. 23 about here.]

6 Conclusions

The main conclusions of this work can be summarized in the following points.

i) The crack propagation in a TCT specimen propagates under mode II except in a transition region located at the centre of the specimen with length proportional to the thickness of the specimen. Therefore care is required when using thick specimen to evaluate the fracture toughness.

ii) Other causes that prevent a pure mode II propagation are the defects near the transverse cut. Micro-CT was able to reveal these defects, and to characterise their shape and entity. The asymmetries found in the materials originate asymmetric crack propagation at the different crack tips and prevent the use of the TCT as a standard test method for the measurement of the interlaminar fracture toughness.

iii) A new geometry is proposed and validated. This new geometry represents an improvement on the classical TCT specimens because it limits all the main causes that prevent a pure mode II propagation.

iv) A difference is found when comparing the values of fracture toughness measured using both the TCT and the ENF specimens. Even though the fracture toughness is a material parameter it is common knowledge that it may depend on the size and on the shape of the specimen. If the dependence on the size may be eliminated, or at least reduced, using the size effect method, the dependence on the shape of the specimen is harder to eliminate and still object of research. It has been postulated here that the difference in the fracture toughness is due to the fact that the TCT tends to measure the steady state value of the R-curve (the fracture toughness in the strict sense of the word) while the ENF derives a value of the fracture toughness that correspond to a point in the rising part of the R-curve. In the authors' opinion, it would also be worth investigating the crack propagation using computational micromechanics. Taking into account the micro-structure of the material could be the key to explain the diverging values of the fracture toughness obtained using the ENF or the TCT.

v) Two experimental techniques, DIC and TSA, have been successfully implemented to evaluate the full field strain/stress distribution in the thickness face around the transverse cut. DIC in particular was useful to reveal the locations and instants of delamination onsets, allowing to observe that the TCT has a tendency to develop unsymmetrical delamination fronts which hamper the derivation of the fracture energy at the critical load. DIC and TSA under quasi-static monotonic loading both showed that the modified TCT geometry has instead a tendency to develop four symmetrical and simultaneous delamination fronts as required by the test. TSA was particularly useful to evidence the tendency of the TCT geometry to develop local randomly distributed stress concentrations near the cut tips, as well as developing dissipation effects probably due to a frictional sliding between plies at the transverse crack. On the contrary, the modified TCT geometry showed a good symmetry of stress distribution, the presence of weak frictional effects near the delamination ends and a thermoelastic signal compatible with a pure mode II near the delamination tips. These results were confirmed by the SEM analyses performed on the fracture surfaces.

vi) The obtained results represent a significant contribution in the understanding of the TCT test as a mode II characterization procedure and provide new guidelines to characterize the mode II crack propagation under tensile loads.

Acknowledgement

The authors would like to acknowledge the Mediterranean Center for Human Health Advanced Biotechnologies (CHHAB, Palermo, Italy) for the assistance with the Micro-CT scans, the Netherlands Technology Foundation (STW) for financial support (under grant 12502), and the funding of Project NORTE-01-0145-FEDER-000022 - SciTech - Science and Technology for Competitive and Sustainable Industries, cofinanced by Programa Operacional Regional do Norte (NORTE2020), through Fundo Europeu de Desenvolvimento Regional (FEDER).

References

[1] Camanho PP and Dávila CG. Mixed-mode decohesion finite elements for the simulation of delamination in composite materials. Technical report, NASA, National Aeronautics and Space Administration, 2002.

[2] P. P. Camanho, C. G. Dávila, and M. F. de Moura. Numerical simulation of mixed-mode progressive delamination in composite materials. *Journal of Composite Materials*, 37(16):1415–1438, 2003.

[3] A. Turon, P.P. Camanho, J. Costa, and C.G. Dávila. A damage model for the simulation of delamination in advanced composites under variable-mode loading. *Mechanics of Materials*, 38(11):1072 – 1089, 2006.

[4] A. Turon, C.G. Dávila, P.P. Camanho, and J. Costa. An engineering solution for mesh size effects in the simulation of delamination using cohesive zone models. *Engineering Fracture Mechanics*, 74(10):1665 – 1682, 2007.

[5] A. Turon, P.P. Camanho, J. Costa, and J. Renart. Accurate simulation of delamination growth under mixed-mode loading using cohesive elements: Definition of interlaminar strengths and elastic stiffness. *Composite Structures*, 92(8):1857 – 1864, 2010.

[6] ASTM D5528-13, Standard Test Method for Mode I Interlaminar Fracture Toughness of Unidirectional Fiber-Reinforced Polymer Matrix Composites, 2013.

[7] ASTM D7905 / D7905M-14, Standard Test Method for Determination of the Mode II Interlaminar Fracture Toughness of Unidirectional Fiber-Reinforced Polymer Matrix Composites, 2014.

[8] ISO 15114:2014. Fibre-reinforced plastic composites – Determination of the mode II fracture resistance for unidirectionally reinforced materials using the calibrated end-loaded split (C-ELS) test and an effective crack length approach. Standard, International Organization for Standardization, Geneva, CH, 2014.

[9] ASTM D6671 / D6671M-13e1, Standard Test Method for Mixed Mode I-Mode II Interlaminar Fracture Toughness of Unidirectional Fiber Reinforced Polymer Matrix Composites, 2013.

[10] Reeder JR and Rews JH. Mixed-mode bending method for delamination testing. *AIAA Journal*, 28(7):1270–1276, Jul 1990.

[11] Davidson BD and Sun X. Effects of Friction, Geometry, and Fixture Compliance on the Perceived Toughness from Three-and Four-Point Bend End-Notched Flexure Tests. *Journal of Reinforced Plastics and Composites*, 24(15):1611–1628, 2005.

[12] SW Dean, BD Davidson, and X Sun. Geometry and data reduction recommendations for a standardized end notched flexure test for unidirectional composites. *J. ASTM Int.*, 3(9):100285, 2006.

[13] Carlos L. Perez and Barry D. Davidson. Evaluation of precracking methods for the end-notched flexure test. *AIAA Journal*, 45(11):2603–2611, nov 2007.

[14] S. W. Dean, Barry D. Davidson, and Sean S. Teller. Recommendations for an ASTM standardized test for determining GIIc of unidirectional laminated polymeric matrix composites. *J. ASTM Int.*, 7(2):102619, 2010.

[15] Prinz R. Ermittlung der Energiefreisetzungsraten GIc und GIIc für das CFK-Laminat M40/Code69. Internal document IB-131-89/34, German Aerospace Center, 1989. in German.

[16] Prinz R and Gädke M. Characterization of interlaminar mode I and mode II fracture in CFRP laminates. In *Proceedings of international conference on spacecraft structures and mechanical testing*, pages 97–102, 1991.

[17] Fink A, Camanho PP, Andrés JM, Pfeiffer E, and Obst A. Hybrid cfrp/titanium bolted joints: Performance assessment and application to a spacecraft payload adaptor. *Composites Science and Technology*, 70(2):305 – 317, 2010.

[18] Wisnom MR. On the increase in fracture energy with thickness in delamination of unidirectional glass fibre-epoxy with cut central plies. *Journal of Reinforced Plastics and Composites*, 11(8):897–909, 1992.

[19] Cui W, Wisnom MR, and Jones M. An Experimental and Analytical Study of Delamination of Unidirectional Specimens with Cut Central Plies. *Journal of Reinforced Plastics and Composites*, 13(8):722–739, 1994.

[20] FP van der Meer and LJ Sluys. A numerical investigation into the size effect in the transverse crack tensile test for mode II delamination. *Composites Part A: Applied Science and Manufacturing*, 54:145–152, 2013.

[21] Catalanotti G, Xavier J, and Camanho PP. Measurement of the compressive crack resistance curve of composites using the size effect law . *Composites Part A: Applied Science and Manufacturing*, 56:300 – 307, 2014.

[22] Blaber J, Adair B, and Antoniou A. Ncorr: Open-source 2d digital image correlation matlab software. *Experimental Mechanics*, 55(6):1105–1122, 2015.

[23] Scalici T, Fiore V, Orlando G, and Valenza A. A dic-based study of flexural behaviour of roving/mat/roving pultruded composites. *Composite Structures*, 131:82–89, 2015.

[24] Scalici T, Pitarresi G, Valenza A, Catalanotti G, and Camanho PP. Experimental evaluation of through-the-thickness stress distribution in transverse crack tension test samples. In *Proceedings of the 20th International Conference on Composite Materials, Copenhagen, 19-24th July 2015*, 2015.

[25] Erçin GH, Camanho PP, Xavier J, Catalanotti G, Mahdi S, and Linde P. Size effects on the tensile and compressive failure of notched composite laminates. *Composite Structures*, 96:736 – 744, 2013.

[26] Catalanotti G, Camanho PP, Xavier J, Dávila CG, and Marques AT. Measurement of resistance curves in the longitudinal failure of composites using digital image correlation. *Composites Science and Technology*, 70(13):1986 – 1993, 2010. ICCM-17: Composites In Biomedical Applications.

[27] Boyd SW, Dulieu-Barton JM, Thomsen OT, and El-Gazzani S. Through thickness stress distributions in pultruded GRP materials. *Composite Structures*, 92(3):662 – 668, 2010.

[28] Pitarresi G and Patterson EA. A review of the general theory of thermoelastic stress analysis. *The Journal of Strain Analysis for Engineering Design*, 38(5):405–417, 2003.

[29] Wong AK, Rajic N, and Nguyen Q. 50th anniversary article: Seeing stresses through the thermoelastic lensa retrospective and prospective from an australian viewpoint. *Strain*, 51(1):1–15, 2015.

[30] Pitarresi G and Galietti U. A Quantitative Analysis of the Thermoelastic Effect in CFRP Composite Materials. *Strain*, 46(5):446–459, 2010.

[31] Emery TR, Dulieu-Barton JM, Earl JS, and Cunningham PR. A generalised approach to the calibration of orthotropic materials for thermoelastic stress analysis. *Composites Science and Technology*, 68(34):743 – 752, 2008.

[32] Pitarresi G. Lock-In Signal Post-Processing Techniques in Infra-Red Thermography for Materials Structural Evaluation. *Experimental Mechanics*, 55(4):667–680, 2013.

[33] P. Brémond and P. Potet. Lock-in Thermography: A Tool to Analyze and Locate Thermomechanical Mechanisms in Materials and Structures. In *Proceedings of SPIE 4360, Thermosense XXIII, Orlando, FL, USA, 23 March 2001*, pages 560–566, 2001.

[34] Colombo C, Vergani L, and Burman M. Static and fatigue characterisation of new basalt fibre reinforced composites . *Composite Structures*, 94(3):1165 – 1174, 2012.

[35] Pitarresi G, Tumino D, and Mancuso A. Thermo-Mechanical Behaviour of Flax-Fibre Reinforced Epoxy Laminates for Industrial Applications. *Materials*, 8(11):5384, 2015.

[36] Suo Z, Bao G, Fan B, and Wang TC. Orthotropy rescaling and implications for fracture in composites. *International Journal of Solids and Structures*, 28(2):235 – 248, 1991.

[37] Bao G, Ho S, Suo Z, and Fan B. The role of material orthotropy in fracture specimens for composites. *International Journal of Solids and Structures*, 29(9):1105–1116, 1992.

[38] Krueger R. Virtual crack closure technique: History, approach, and applications. *Applied Mechanics Reviews*, 57(2):109–143, Apr 2004.

[39] Dassault Systèmes, Providence, RI, USA. *ABAQUS Documentation*.

[40] Bazant ZP and Planas J. *Fracture and Size Effect in Concrete and Other Quasibrittle Materials*. New Directions in Civil Engineering. Taylor & Francis, 1997.

[41] Catalanotti G and Xavier J. Measurement of the mode II intralaminar fracture toughness and R-curve of polymer composites using a modified Iosipescu specimen and the size effect law . *Engineering Fracture Mechanics*, 138:202–214, 2015.

[42] Catalanotti G, Arteiro A, Hayati M, and Camanho PP. Determination of the mode i crack resistance curve of polymer composites using the size-effect law. *Engineering Fracture Mechanics*, 118:49 – 65, 2014.

[43] Catalanotti G, Xavier J, and Camanho PP. Measurement of the compressive crack resistance curve of composites using the size effect law. *Composites Part A: Applied Science and Manufacturing*, 56:300 – 307, 2014.

[44] Pitarresi G, Alessi S, Tumino D, Nowicki A, and Spadaro G. Interlaminar fracture toughness behavior of electron-beam cured carbon-fiber reinforced epoxy resin composites. *Polymer Composites*, 35(8):1529–1542, 2014.

[45] Drzal LT and Madhukar M. Fibre-matrix adhesion and its relationship to composite mechanical properties. *Journal of Materials Science*, 28(3):569–610, 1993.

[46] Roger M.L. Foote, Yiu-Wing Mai, and Brian Cotterell. Crack growth resistance curves in strain-softening materials. *Journal of the Mechanics and Physics of Solids*, 34(6):593 – 607, 1986.

[47] O'Brien TK, Johnston WM, and Toland GJ. Mode II Interlaminar Fracture Toughness and Fatigue Characterization of a Graphite Epoxy Composite Material. Technical Report NASA/TM–2010-216838, NASA – National aeronautics and space administration, 2010.

[48] Camanho PP, Tavares CML, Almeida JB, Bandeira PM, Portela PM, Melro A, de Oliveira R, and Figueiredo M. Inserts for cfrp structures – technical note 4. unpublished.

[49] P.P. Camanho, P. Maimí, and C.G. Dávila. Prediction of size effects in notched laminates using continuum damage mechanics. *Composites Science and Technology*, 67(13):2715 – 2727, 2007.

List of Figures

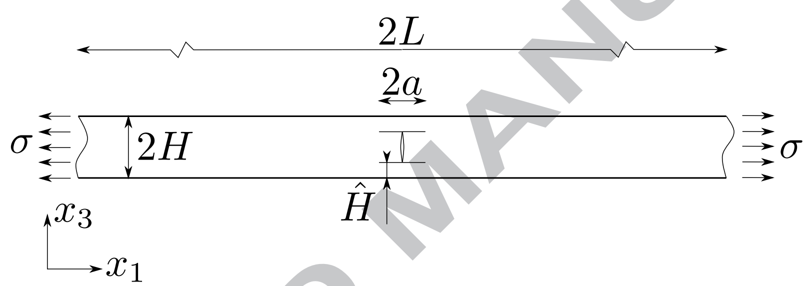

Fig. 1. TCT specimen: geometrical parameters and coordinate system.

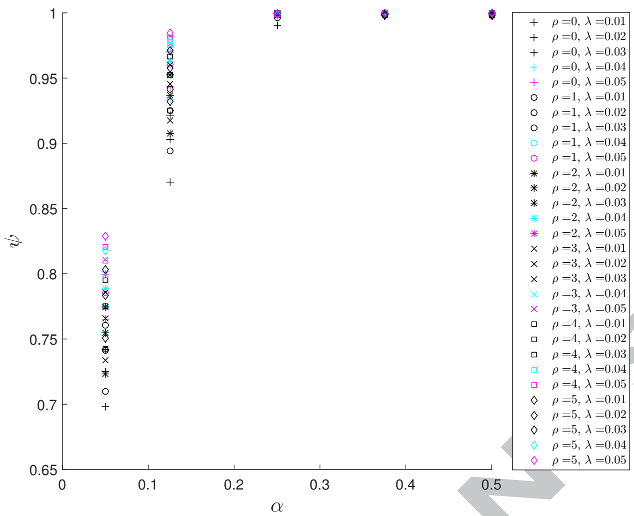

(a) ψ vs. α

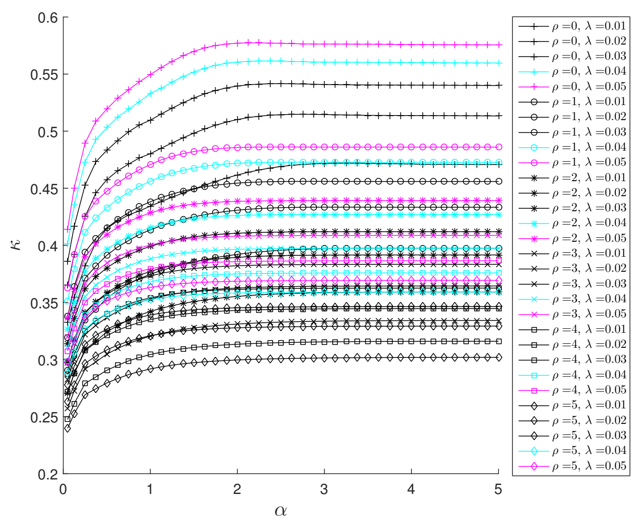

(b) κ vs. α

Fig. 2. Mode mixity ψ and correction factor κ as a function of α.

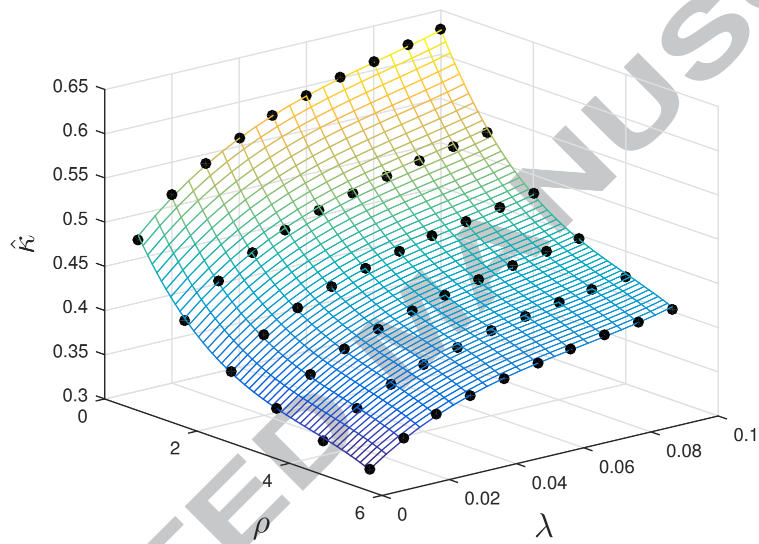

Fig. 3. $\hat{\kappa}$ as a function of λ and ρ: numerical results (red dots) and polynomial fitting.

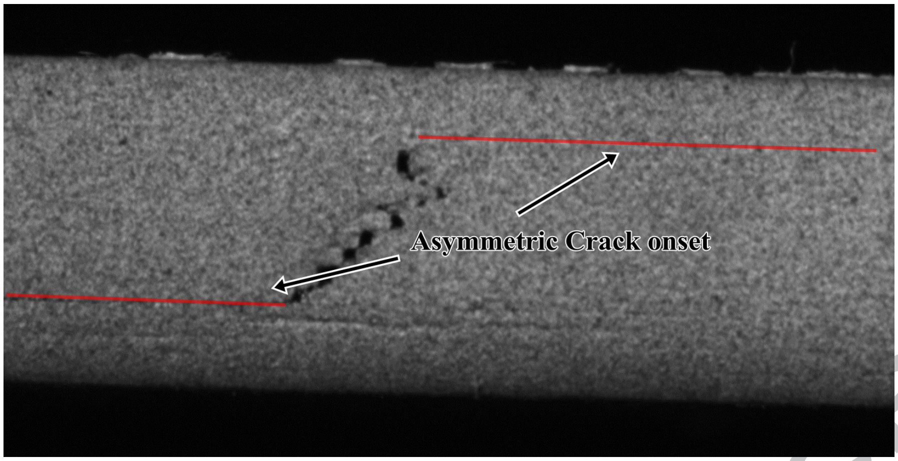

Fig. 4. Asymmetrical crack onset.

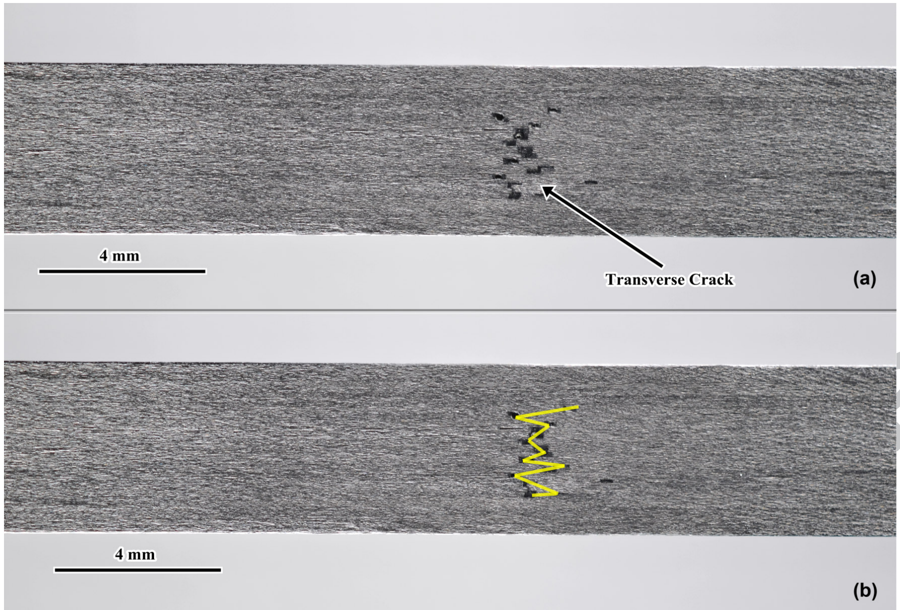

Fig. 5. crack macrography: (a) real picture; (b) crack morphology

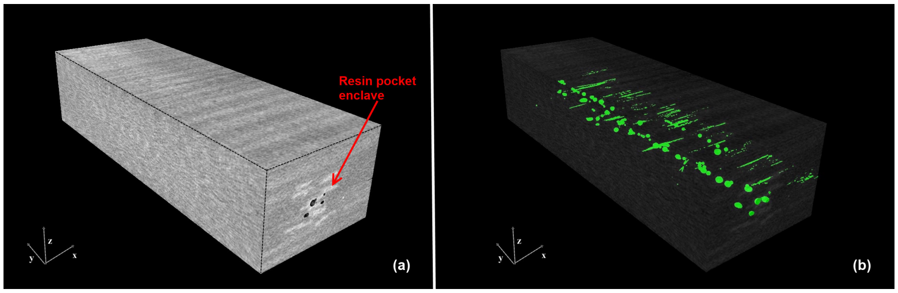

Fig. 6. Micro-CT: (a) 3D reconstruction; (b) Defects distribution

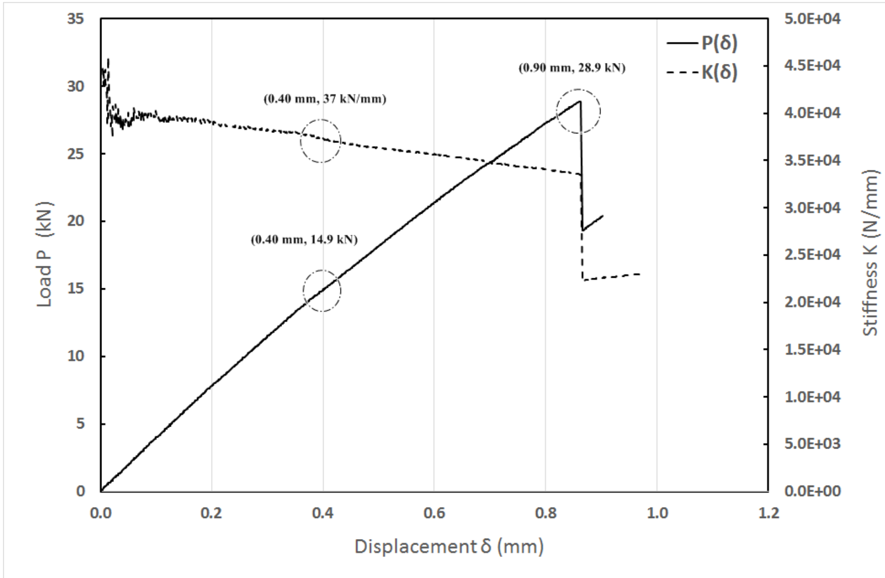

Fig. 7. Typical load vs. displacement curve and stiffness vs. displacement curve obtained in a TCT test

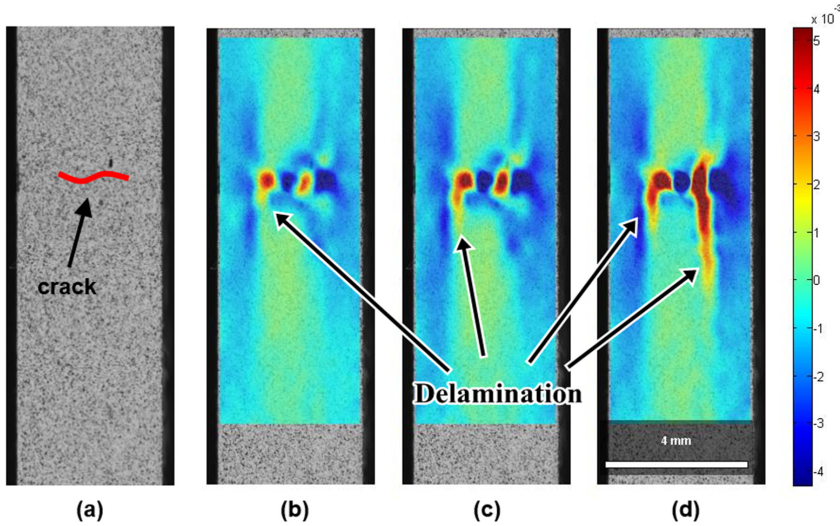

Fig. 8. DIC Results at different loads: (a) Reference image; (b) 22.4 kN; (c) 30kN; (d) 31 kN

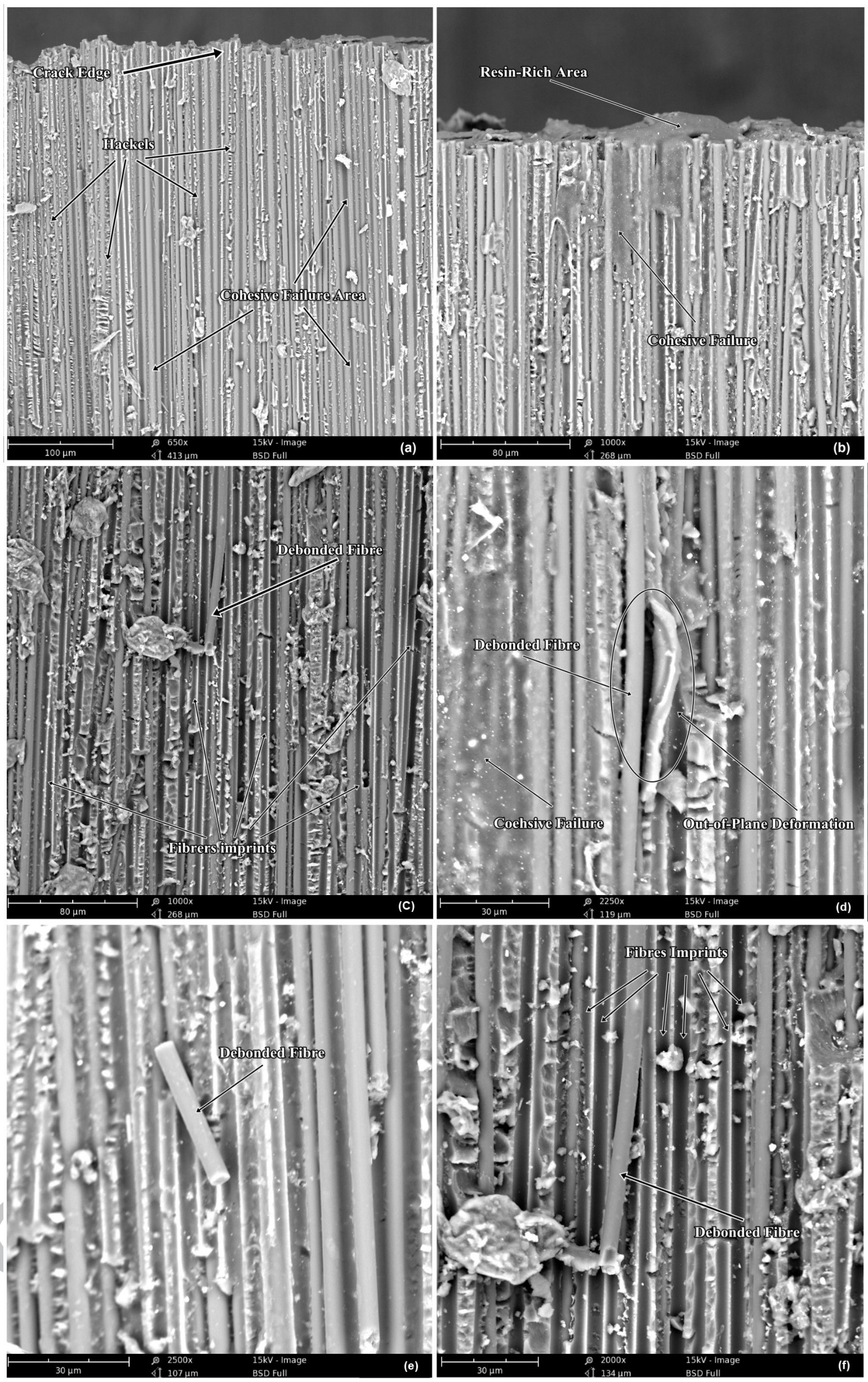

Fig. 9. SEM: (a) close-to-crack overviews; (b) Resin Rich Area; (c) (d) (e) (f) Debonded fibre and fibre imprints.

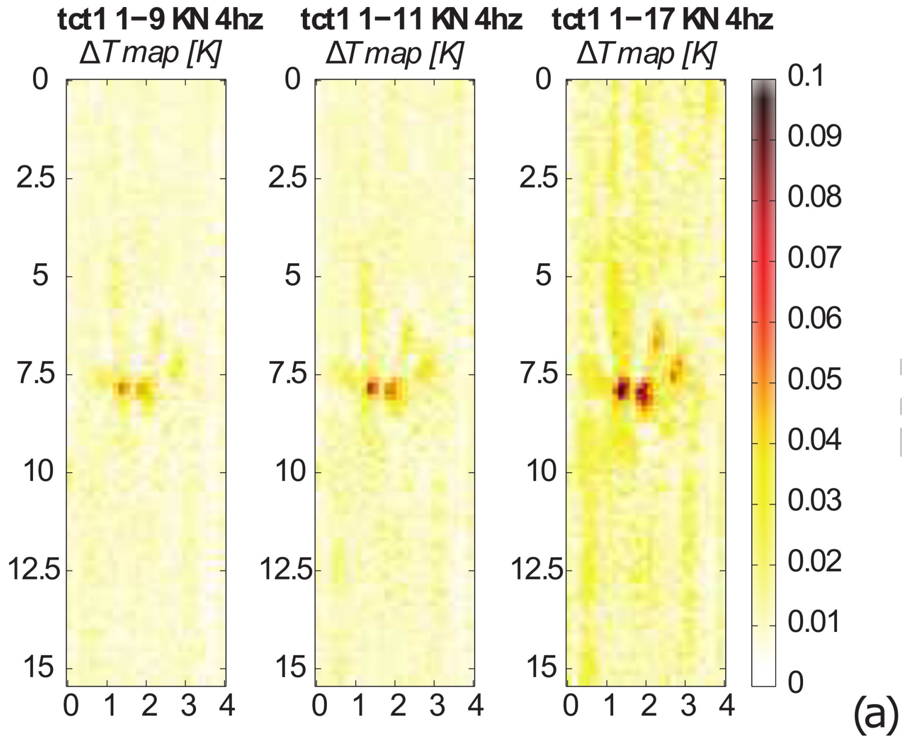

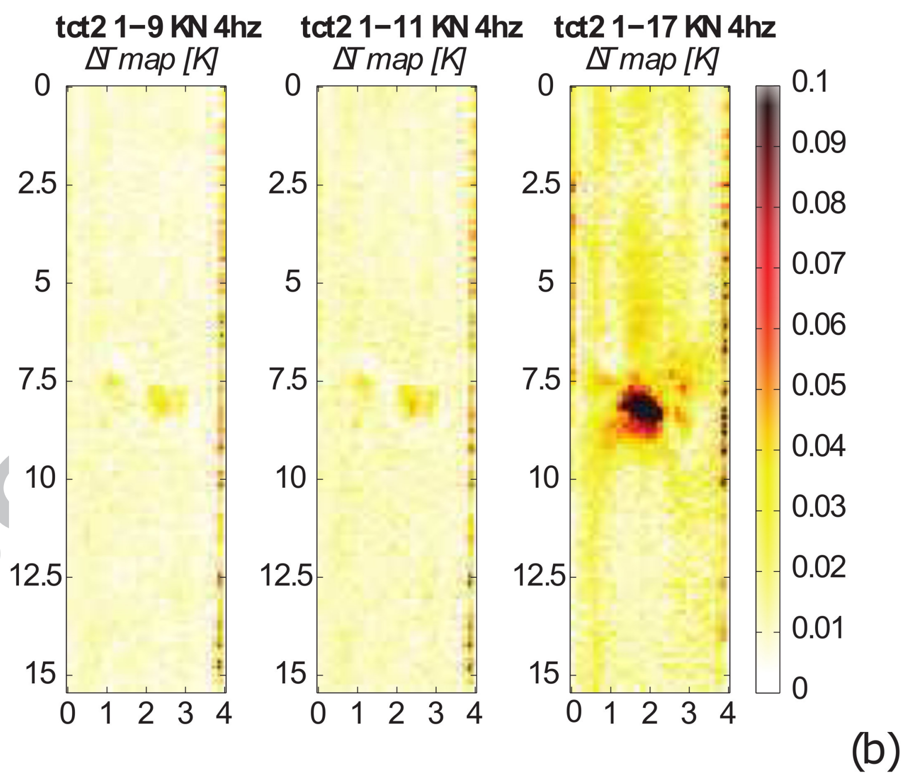

Fig. 10. TSA: (a) Thermoelastic signal amplitude at varying the load amplitude for the sample `tct1`; (b) Thermoelastic signal amplitude at varying the load amplitude for the sample `tct2`.

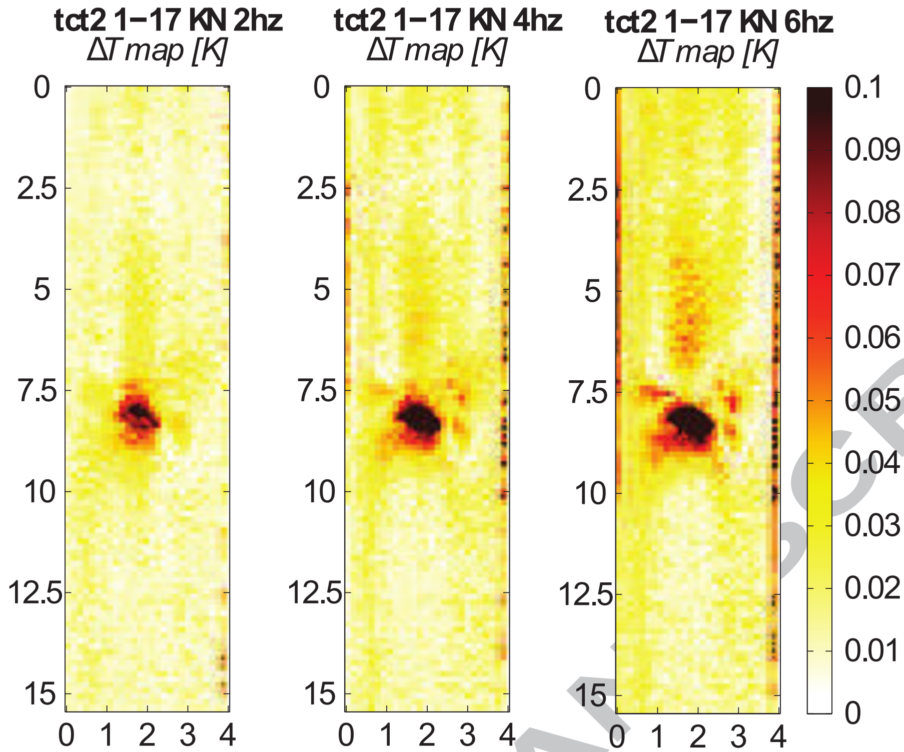

Fig. 11. TSA: Thermoelastic signal amplitude at varying the load frequency for the sample `tct2`

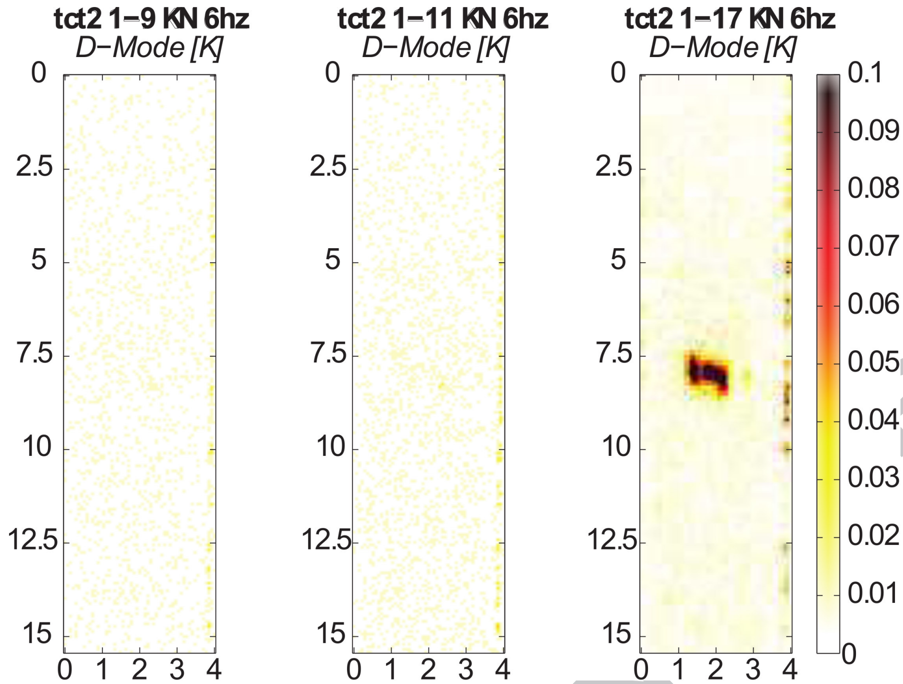

Fig. 12. TSA: Dissipation maps at varying the load amplitude

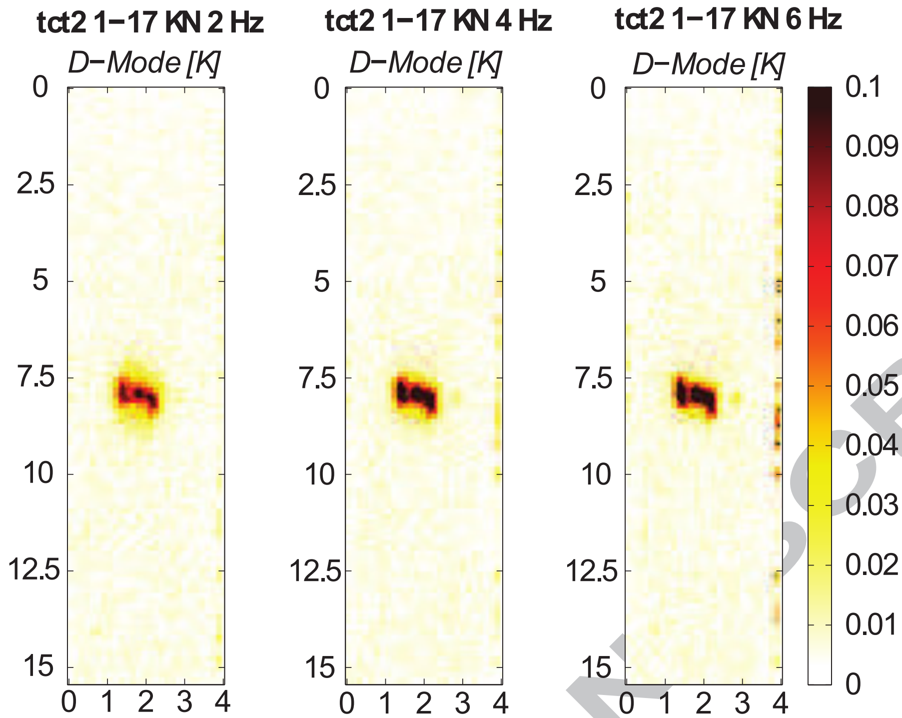

Fig. 13. TSA: Dissipation maps at varying the load frequency

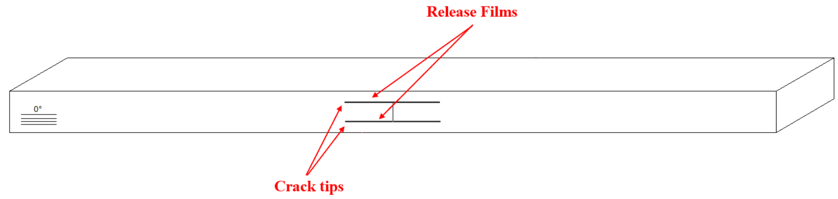

Fig. 14. A new configuration – proposed geometry

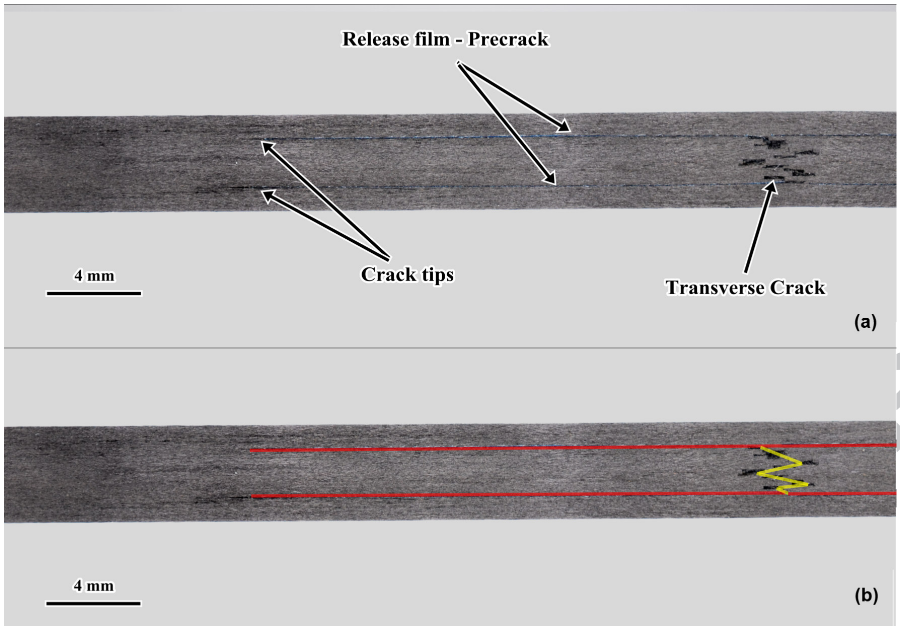

Fig. 15. A new configuration – (a) macrography; (b) crack geometry.

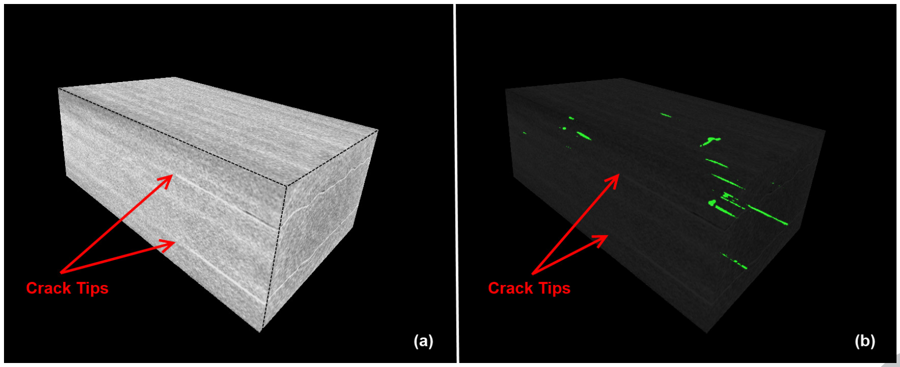

Fig. 16. A new configuration – Micro-CT: (a) 3D reconstruction; (b) Defects distribution

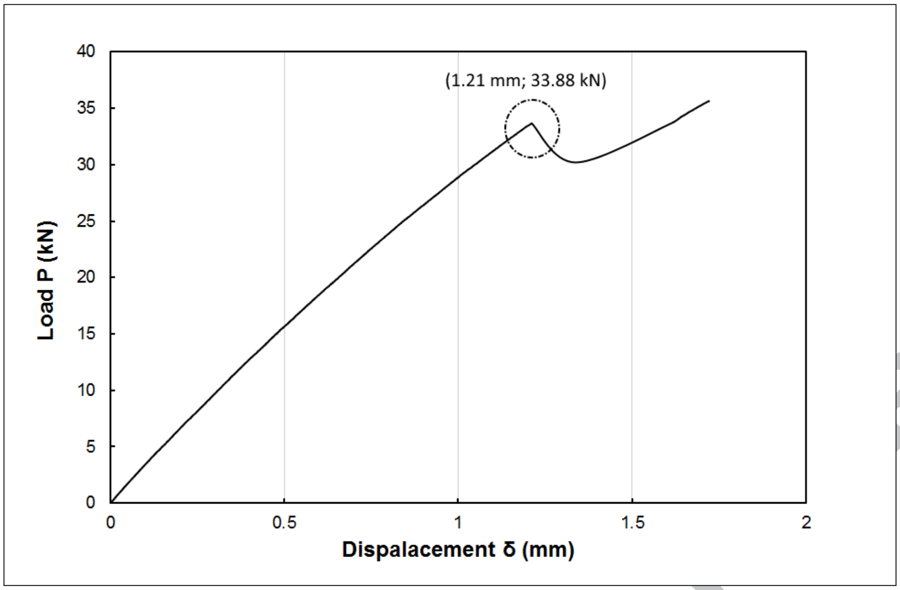

Fig. 17. A new configuration – Typical load vs. displacement curve and stiffness vs. displacement curve

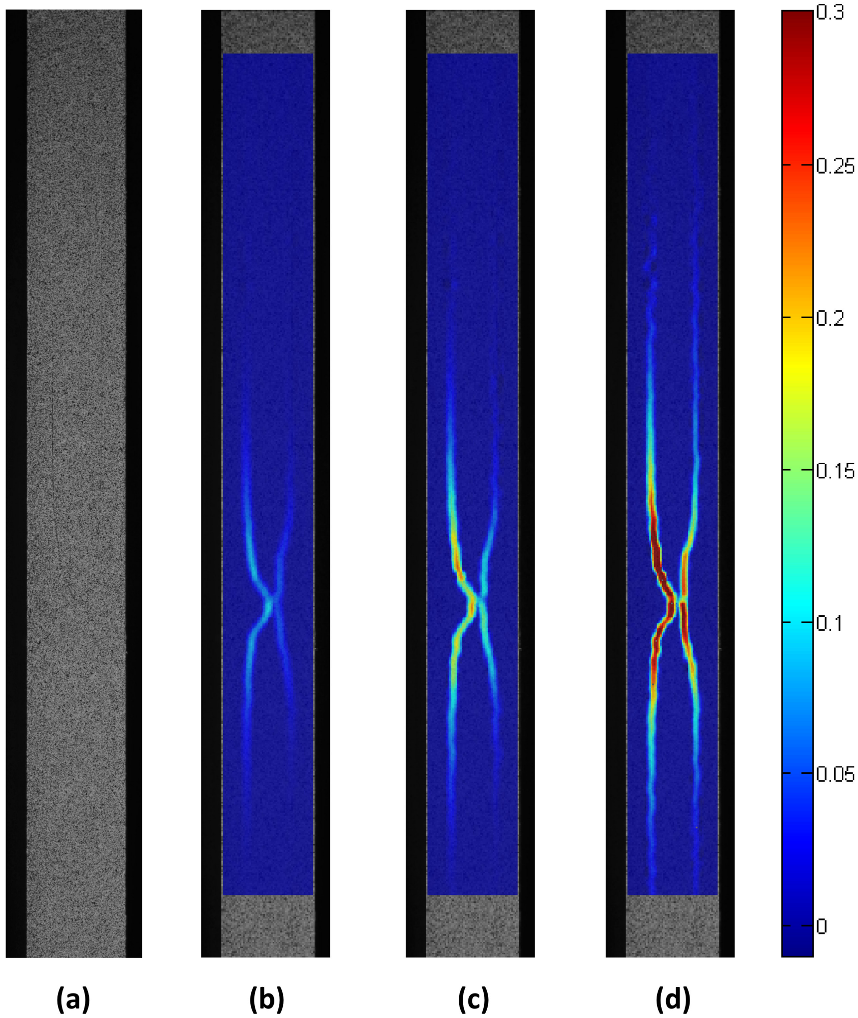

Fig. 18. A new configuration - DIC Results at different load level: (a) Reference Image; (b) 7.5 kN; (c) 15.8 kN; (d) 33.2 kN

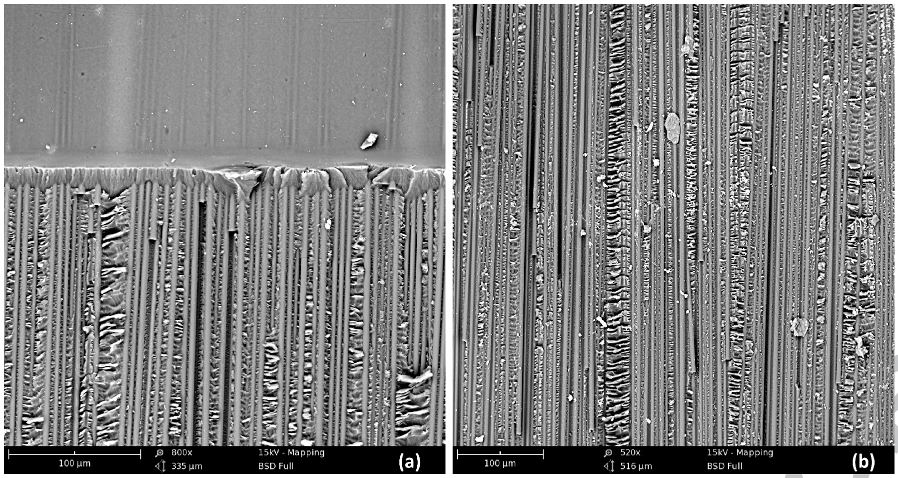

Fig. 19. A new configuration SEM: (a) Crack tip; (b) Crack surface overview

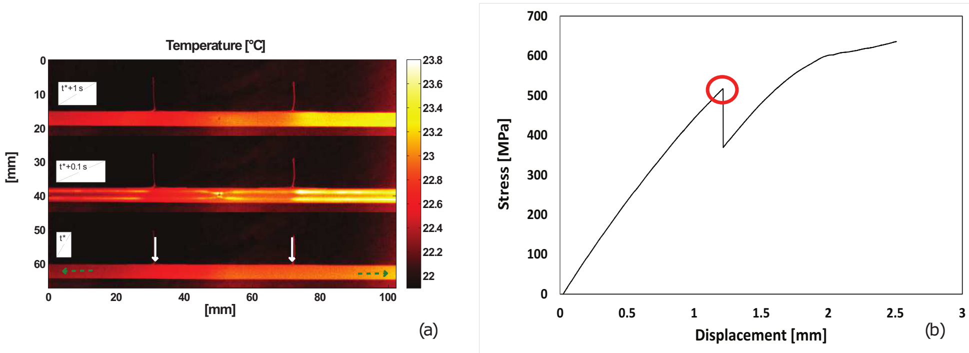

Fig. 20. A new configuration – Monotonic Loading: (a) thermograms sequence during the failure (b) typical stress vs. displacement curve

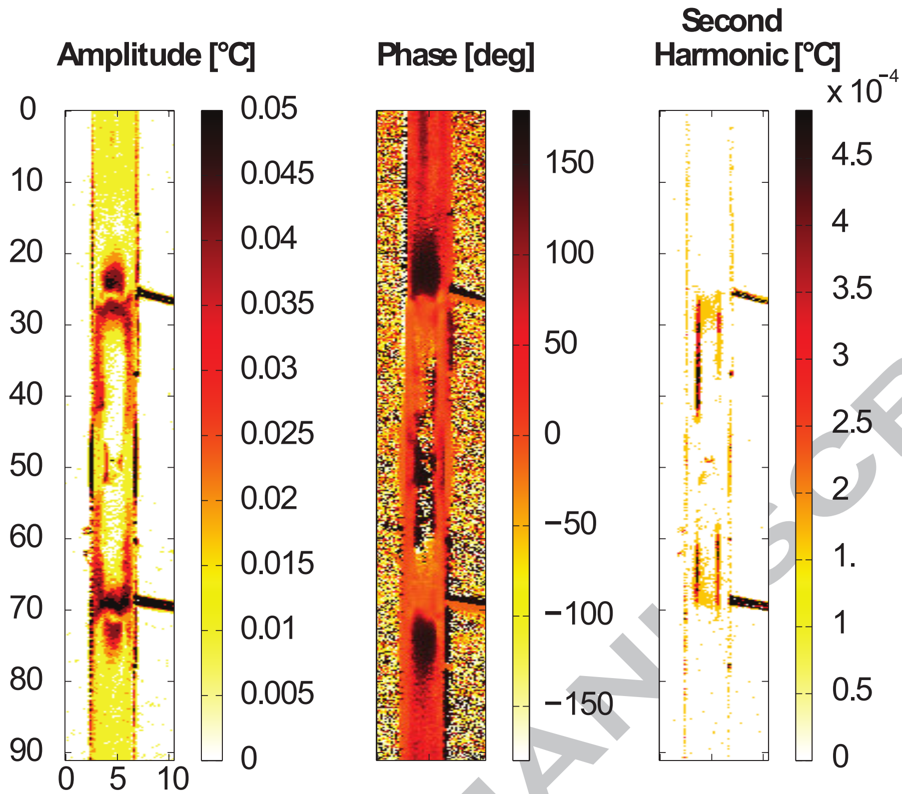

Fig. 21. A new configuration – Thermoelastic amplitude, phase and dissipation mode for 4-21 kN/4 Hz loaded sample

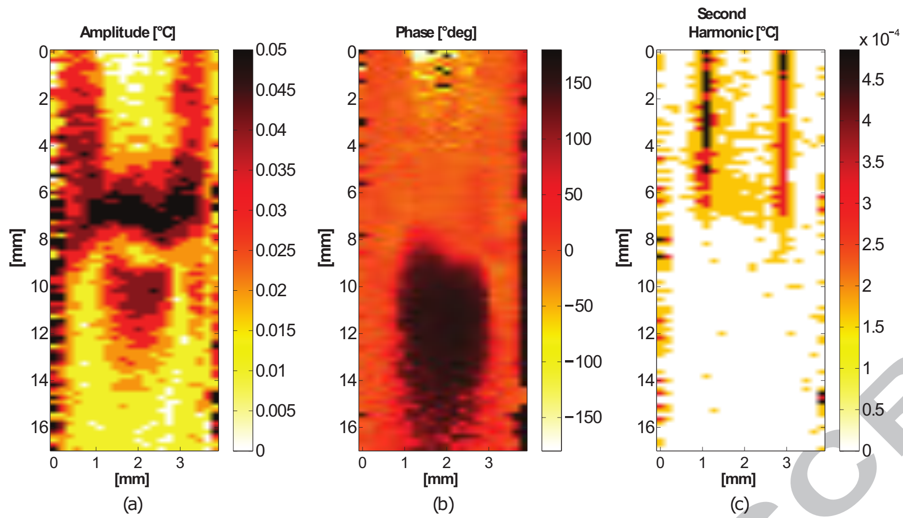

Fig. 22. A new configuration – Thermoelastic amplitude, phase and dissipation mode for a 4-21 kN/4 Hz loaded sample: a close up on the crack tips

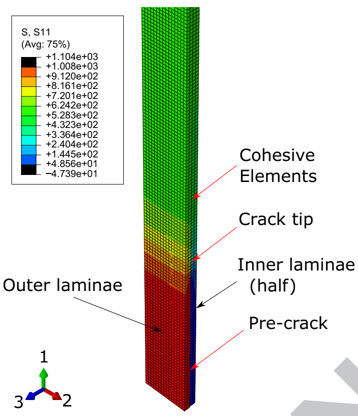

(a) FE model of the mTCT specimen (one eighth).

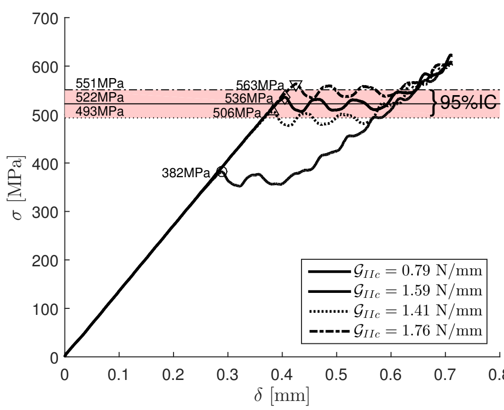

(b) Remote stress, σ, vs. displacement, δ, and comparison with experiments.

Fig. 23. FE model results.

List of Tables

Table 1
Properties of the cured Hexcel IM7-8552 unidirectional lamina

E_1 [MPa]	171420
E_2 [MPa]	9080
G_{12} [MPa]	5290
ν_{12} [–]	0.32
α_{11} [1/K]	-5.5×10^{-6}
α_{22} [1/K]	25.8×10^{-6}

Table 2
Photomechanic setup

Camera type	Single-lens digital reflex
Image sensor	23.5×15.6 mm CMOS
Effective Pixel	24.1 MPixel
Focal Lengh	60 mm - macro
Sampling Rate	0.5 Hz
Resultant resolution	20 μm/mm
Subset Radius	20 pixel
Subset Overlapping	5 pixel
Displacement rate	2 mm/sec

Table 3
Failure mode of the TCTs specimens tested

Sample ID	H [mm]	h [mm]	P_u [kN]	Failure mode
TCT-1-1	1.5	0.75	17.5	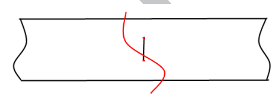
TCT-1-2	1.5	0.75	17.2	
TCT-1-3	1.5	0.75	17.4	
TCT-1-4	1.5	0.75	17.3	
TCT-2-1	3.0	1.5	24.2	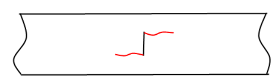
TCT-2-2	3.0	1.5	25.3	
TCT-2-3	3.0	1.5	26.2	
TCT-2-4	3.0	1.5	24.5	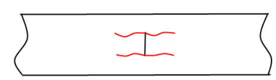
TCT-3-1	4.5	2.25	27.7	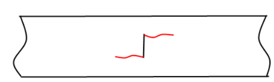
TCT-3-2	4.5	2.25	27.8	
TCT-3-3	4.5	2.25	27.0	
TCT-3-4	4.5	2.25	27.2	

Table 4
Mode II Fracture Toughness

	1	2	3	4	Mean	St.Dev.
δ_c [mm]	1.22	0.96	1.17	1.21	1.14	0.11
σ_c [MPa]	517	498	538	535	522	18
$\mathcal{G}_{IIc}$ [N/mm] (Eq. (4))	1.56	1.44	1.68	1.66	1.59	0.11
$\mathcal{G}_{IIc}$ [N/mm] (Eq. (9))	1.57	1.46	1.70	1.68	1.60	0.11

Table 5
Interlaminar material properties

	Material property	Value or calculation method	Ref.
K [N/mm^3]	Penalty stiffness	10^6	[2]
τ_N [MPa]	Effective strength in pure mode I	Eq. (13)	[4]
τ_{sh} [MPa]	Effective strength in pure mode II	Eq. (14)	[5]
$\mathcal{G}_{Ic}$ [N/mm]	Mode I fracture toughness	0.28	[48]
$\mathcal{G}_{IIc}$ [N/mm]	Mode II fracture toughness	0.79, 1.59, 1.41, 1.76	[48]